Central Lancashire Online Knowledge (CLoK)

Title	Near-infrared spectroscopic indices for unresolved stellar populations. III. Composite indices definition as age and metallicity tracers and model comparison
Type	Article
URL	https://clok.uclan.ac.uk/51076/
DOI	##doi##
Date	2024
Citation	Gasparri, D, Morelli, L, Cuomo, V, Ivanov, V D, Pizzella, A, François, P, Coccato, L, Corsini, E M, Costantin, L et al (2024) Near-infrared spectroscopic indices for unresolved stellar populations. III. Composite indices definition as age and metallicity tracers and model comparison. Monthly Notices of the Royal Astronomical Society, 530 (1). pp. 560-585. ISSN 0035-8711
Creators	Gasparri, D, Morelli, L, Cuomo, V, Ivanov, V D, Pizzella, A, François, P, Coccato, L, Corsini, E M, Costantin, L, Bontà, Elena Dalla, Méndez-Abreu, J and Aguerri, J A L

It is advisable to refer to the publisher's version if you intend to cite from the work. ##doi##

For information about Research at UCLan please go to http://www.uclan.ac.uk/research/

Near-infrared spectroscopic indices for unresolved stellar populations. III. Composite indices definition as age and metallicity tracers and model comparison

D. Gasparri [ORCID],[1] L. Morelli,[1,2]★ V. Cuomo [ORCID],[1] V. D. Ivanov,[3,4] A. Pizzella [ORCID],[5,6] P. François,[7] L. Coccato [ORCID],[3]
E. M. Corsini [ORCID],[5,6] L. Costantin,[8] E. Dalla Bontà [ORCID],[5,6,9]† J. Méndez-Abreu [ORCID][10,11] and J. A. L. Aguerri[10,11]

[1]*Instituto de Astronomía y Ciencias Planetarias, Universidad de Atacama, Copayapu 485, Copiapó, Chile*
[2]*INAF – Osservatorio Astronomico di Brera, via Brera 28, I-20121 Milano, Italy*
[3]*European Southern Observatory, Karl-Schwarzschild-Strasse 2, D-85748 Garching bei München, Germany*
[4]*European Southern Observatory, Avenida Alonso de Córdova 3107, Vitacura, Santiago, Chile*
[5]*Dipartimento di Fisica e Astronomia 'G. Galilei', Università di Padova, vicolo dell'Osservatorio 3, I-35122 Padova, Italy*
[6]*INAF – Osservatorio Astronomico di Padova, vicolo dell'Osservatorio 5, I-35122 Padova, Italy*
[7]*GEPI, Observatoire de Paris, PSL Research University, CNRS, Université Paris Diderot, Sorbonne Paris Cité, 61 Avenue de l'Observatoire,*
F-75014 Paris, France
[8]*Centro de Astrobiología (CAB), CSIC-INTA, Ctra de Ajalvir km 4, Torrejón de Ardoz, E-28850 Madrid, Spain*
[9]*Jeremiah Horrocks Institute, University of Central Lancashire, Preston, PR1 2HE, UK*
[10]*Instituto Astrofísico de Canarias, C/ Vía Láctea s/n, E-38200 La Laguna, Spain*
[11]*Departamento de Astrofísica, Universidad de La Laguna, C/ Astrofísico Francisco Sánchez, E-38205 La Laguna, Spain*

ABSTRACT
Recent advances in the stellar population studies of unresolved galaxies in the NIR domain demonstrated that it contains several line-strength indices to be potentially used as diagnostics for stellar population properties. Reduction of the extinction and possibility to disentangle different stellar populations dominating different spectral ranges are obviously beneficial. To this aim, we have investigated the connections between 19 Lick/IDS indices and 39 NIR indices measured in the central regions of 32 galaxies observed with X-shooter. We adopted a systematic approach to deriving a correlation matrix using all the optical and NIR indices measured for the galaxies and building new NIR composite indices to maximize their correlations with the best age and metallicity optical tracers. We found that the new T1 and [AlFeCr] composite indices are promising age and metallicity diagnostics in NIR, respectively. We finally tested the T1 and [AlFeCr] indices with the predictions of simple stellar populations models, and we found that the models show a general agreement with the data. Some fine tuning and further comparison between models and data, which are now largely available, is necessary to reach the prediction level of the optical line-strength indices.

Key words: galaxies: abundances – galaxies: evolution – galaxies: formation – galaxies: stellar content – infrared: galaxies.

1 INTRODUCTION

The definition of Lick/IDS line-strength indices (Burstein et al. 1984; Faber et al. 1985; Worthey et al. 1994; Worthey & Ottaviani 1997) and the improving quality of the simple stellar population (SSP) models (Thomas, Maraston & Bender 2003; Schiavon 2007; Johansson, Thomas & Maraston 2010; Vazdekis et al. 2010; Maraston & Strömbäck 2011; Vazdekis et al. 2015; Conroy et al. 2018; Maraston et al. 2020; Knowles et al. 2021) were fundamental to our knowledge of the stellar content of galaxies (e.g. Trager et al. 1998, 2000; Sánchez-Blázquez et al. 2006; Morelli et al. 2015, 2016; Corsini et al. 2018; Costantin et al. 2018; Martín-Navarro et al. 2018; Costantin et al. 2019; Ditrani et al. 2023).

In the last three decades, many authors systematically explored the existence of stellar population diagnostics in the NIR.

Early works on the strongest NIR spectral absorption features date back to the 1980s (e.g. Rieke et al. 1980). In the 1990s, some authors investigated the NIR absorption lines/bands as possible proxies to constrain the properties of the stellar populations of galaxies and globular clusters (e.g Silva et al. 1994; Oliva et al. 1995; Origlia et al. 1997) focusing to the CO molecular bands, the strong Si line at 1.59 μm and the Brγ line at 2.16 μm.

In the 2000s, Cenarro et al. (2001) presented a calibration of the strong Calcium Triplet (CaT) index and found an unexpected anticorrelation with the central velocity dispersion of early-type galaxies (Cenarro et al. 2003). Falcón-Barroso et al. (2003) showed that this behaviour also holds for the bulges of spiral galaxies.

Riffel et al. (2007) detected for the first time, the CN bands in active galactic nuclei. Along with the CO bands, they have been considered proof of young/intermediate stellar populations and possible age

★ E-mail: lorenzo.morelli@uda.cl
† Visiting Fellow at UCLan

indicators in the NIR. Riffel et al. (2008) analysed 15 absorption features in the NIR for somewhat limited sample of four starbust galaxies, and demonstrated that some features may trace the stellar formation histories of starbust galaxies. They also extended their study to constrain the star formation in Seyfert galaxies (Riffel et al. 2009).

Silva, Kuntschner & Lyubenova (2008) compared optical and NIR indices finding correlations between the newly defined indices in the K atmospheric window and the optical [MgFe]′ index, suggesting that some of the IR features could be adopted as metallicity diagnostics. These findings were later expanded by Mármol-Queraltó et al. (2009) proposing the D_{CO} index as possible tracer of intermediate-age stellar populations and by Cesetti et al. (2009), who investigated the properties of the two Mg indices in the H atmospheric window. They claimed possible correlations with the optical metallicity indices, but they did not find evidence for a strong age indicator like the Hβ in the optical band, crucial to break the age-metallicity degeneracy. The lack of age indicators in the NIR was then confirmed by Baldwin et al. (2018), which investigated a group of atomic and molecular NIR indices in a small number of galaxies.

Kotilainen et al. (2012) studied some NIR features in the K atmospheric window in high spatial resolution, medium spectral resolution spectra of 29 local and inactive galaxies, concluding that the contribution of stars outside the AGB–RGB branches is negligible for any galaxy, independently of their Hubble type.

Cesetti et al. (2013) carried out the first systematic study to identify, in the NIR spectra of different types of stars, features that would be promising as proxies of the stellar population properties in galaxies. They defined 27 NIR indices in the I and K atmospheric windows using the stellar spectra of the NASA IRTF spectral library (Rayner, Cushing & Vacca 2009) to investigate their sensitivity to the physical properties of stars (T_{eff}, [Fe/H], log g) with the aim of objectively defining sensitive indices to the age and metallicity of unresolved stellar populations. Morelli et al. (2020) complemented this work extending the investigation to spectral features in the 1–5 µm wavelength range. As a result, they identified the best indicators in the Y, J, H, and L atmospheric windows for the different physical parameters of the stars, and for some of the properties of the stellar populations in unresolved galaxies.

Riffel et al. (2019) analysed 40 NIR indices from the I through K atmospheric windows in the spectra of 35 galaxies and compared them with the optical Lick/IDS indices, finding metallicity sensitive features. They also proposed a new index that correlates with the central velocity dispersion.

Additional effort to investigate the spectra of galaxies in the Y, J, and H atmospheric windows was carried out by several authors looking for possible gravity sensitive features to constrain the IMF of galaxies (e.g. La Barbera et al. 2013; Mason et al. 2015; Lagattuta et al. 2017; Baldwin et al. 2018).

A fundamental and complementary ingredient in the study of this topic is the theoretical modelling of the chemical evolution of galaxies. Models can predict the stellar population properties of a galaxy at different stages of its formation and evolution. The development of such models in the optical range advanced well in the last decades (Worthey et al. 1994; Thomas et al. 2003; Johansson et al. 2010; Vazdekis et al. 2010), reaching a very high level of reliability and being able to predict the spectra of galaxies at different epochs. These successes gave a formidable boost to the investigation of galaxy stellar populations from unresolved spectra in the optical wavelength range.

On the opposite, for many years, the greatest limitation for these studies in the NIR was the limited development of theoretical models able to reproduce the properties of the galaxies.

This scenario changed with the theoretical models by Bruzual & Charlot (2003), and the effort made to build reliable semi-empirical models based on early NIR stellar libraries (Mouhcine & Lançon 2002; Maraston 2005). With the increasing number and quality of NIR spectra, large stellar libraries were assembled, either limited to the J, H, and K atmospheric windows (Ivanov et al. 2004) or covering the entire NIR range, like the IRTF spectral libraries (Rayner et al. 2009; Villaume et al. 2017) and the more recent XSL (Arentsen et al. 2019; Gonneau et al. 2020; Verro et al. 2022a). These stellar libraries have been the base for building more complete and reliable SSP models (e.g. Conroy & van Dokkum 2012; Meneses-Goytia et al. 2015; Röck et al. 2016; Vazdekis et al. 2016; Conroy et al. 2018; Verro et al. 2022b).

To date, empirical and theoretical SSP models in the NIR have been widely compared with galaxy spectra and, although there are still small discrepancies with data (Riffel et al. 2011, 2019; Röck et al. 2015, 2016; Vazdekis et al. 2016; Baldwin et al. 2018; Eftekhari et al. 2022), they are extremely helpful in investigating stellar populations.

All these improvements set out the starting point for our observational project. In Gasparri et al. (2021, Paper II hereafter), we presented the results for a sample of 14 galaxy spectra obtained with a high signal-to-noise ratio (S/N) at medium resolution with the X-shooter spectrograph (Guinouard et al. 2006) mounted at the Very Large Telescope (VLT) of the European Southern Observatory (ESO). These spectra simultaneously map the optical and NIR ranges of the galaxy spectral energy distribution, making easier the direct comparison of the spectral properties of unresolved stellar populations at different wavelengths. We compared the NIR line-strength indices defined by Cesetti et al. (2013); Morelli et al. (2020) with the most widely used optical age and metallicity indicators. We found that the NIR Al ($\lambda \sim 1.31$ µm), Al1 ($\lambda \sim 1.67$ µm), CO1 ($\lambda \sim 1.56$ µm), and FeH1 ($\lambda \sim 1.58$ µm) indices are strongly correlated to the optical Mg2 and Mgb indices sensitive to the α/Fe enhancement and with the ⟨Fe⟩ and [MgFe]′ indices sensitive to the total metallicity. Most importantly, the NIR Paβ ($\lambda \sim 1.28$ µm) index, which is tightly correlated with the optical Hβ index sensitive to the mean age of the stellar populations.

To further explore this idea, in this paper, we complemented the galaxy sample of Paper II with 18 additional galaxies. We extended the age and metallicity range to younger and more metal-poor galaxies in order to test our indices and build new composite indices that best correlate to the optical line-strength indices used as age and metallicity diagnostics. Finally, we compared them with the most reliable SSP models now available; the well-tested EMILES (Röck et al. 2015, 2016; Vazdekis et al. 2016), and the new X-shooter (XSL, Verro et al. 2022b) semi-empirical models.

The paper is organized as follows: We present our data set in Section 2. We describe data reduction and analysis in Section 3. We define new NIR composite indices that best correlate with the optical age and metallicity Lick/IDS indicators in Section 4, then we compare them with the optically derived stellar population parameters and with state-of-the-art NIR SSP models available in Section 5. We also define a new NIR composite index correlated to the central velocity dispersion of galaxies in Section 6. Finally, in Section 7 we discuss our conclusions.

Table 1. Properties of the sample galaxies from the HyperLEDA data base (Makarov et al. 2014).

Galaxy ID (1)	Type (2)	T (3)	$\log D_{25} \times \log d_{25}$ (arcmin) (4)	B_T (mag) (5)	A_B^g (mag) (6)	A_B^i (mag) (7)	M_{Bt} (mag) (8)
NGC 0584	E4	−4.7	3.80 × 2.51	11.31	0.18	0	−20.45
NGC 0636	E3	−4.9	2.69 × 2.29	12.35	0.11	0	−19.36
NGC 0897	Sa	1.1	1.99 × 1.41	12.81	0.09	0.14	−21.35
NGC 1357	Sab	1.9	3.38 × 2.57	12.40	0.19	0.15	−19.91
NGC 1425	Sb	3.2	4.78 × 2.09	11.32	0.06	0.53	−20.63
NGC 1600	E3	−4.6	3.09 × 2.00	11.94	0.19	0	−22.21
NGC 1700	E3	−4.7	3.09 × 1.94	12.03	0.19	0	−21.71
NGC 2613	Sb	3.1	7.85 × 1.77	11.11	0.38	0.85	−22.18
NGC 3115	S0	−2.9	7.07 × 3.01	10.08	0.20	0	−20.72
NGC 3377	E5-6	−4.8	3.89 × 1.86	11.13	0.15	0	−19.67
NGC 3379	E5-6	−4.8	4.89 × 4.26	10.23	0.11	0	−20.98
NGC 3423	Sc	6.0	3.54 × 3.01	11.61	0.13	0.12	−19.92
NGC 4415	S0a	−0.9	1.28 × 1.14	13.59	0.09	0	−17.59
NGC 7424	Sc	6.0	5.01 × 2.69	11.05	0.05	0.47	−19.29
NGC 7465	S0	−1.8	1.07 × 0.65	13.36	0.33	0	−19.39
IC 0676	S0	−1.3	1.86 × 1.32	13.41	0.11	0	−18.36
NGC 0516	S0	−1.5	1.62 × 0.47	14.25	0.29	0	−18.82
NGC 4124	S0	−1.3	1.58 × 1.10	12.33	0.12	0	−19.84
NGC 4324	S0	−0.9	2.95 × 1.20	12.40	0.10	0	−19.12
NGC 4643	S0	−0.6	2.24 × 1.74	11.23	0.13	0.01	−20.51
NGC 4684	S0	−1.2	2.88 × 0.93	12.16	0.12	0	−18.71
NGC 5574	S0	−2.8	1.32 × 0.83	13.29	0.13	0	−18.80
NGC 5854	S0	−1.1	3.02 × 0.71	12.65	0.23	0	−19.81
NGC 7693	S0	−1.0	0.83 × 0.51	14.58	0.15	0	−18.45
PGC 56772	S0	−2.0	1.29 × 0.51	14.78	0.19	0	−18.52
NGC 1389	SAB0	−2.8	2.57 × 1.44	12.42	0.05	0	−19.25
NGC 1426	E4	−4.9	2.88 × 1.95	12.27	0.07	0	−19.67
NGC 3818	E5	−4.6	2.45 × 1.55	12.70	0.16	0	−19.87
NGC 4339	E0	−4.6	2.34 × 2.24	12.32	0.11	0	−18.87
NGC 4365	E3	−4.8	5.12 × 3.71	10.50	0.09	0	−21.42
NGC 4371	SB0	−1.3	3.89 × 1.82	11.68	0.16	0	−19.61
NGC 4377	SA0	−2.6	1.58 × 1.23	12.68	0.17	0	−18.72

Col (1): Galaxy name. Col. (2): Hubble morphological type. Col. (3): Morphological stage. Col. (4): Major and minor isophotal diameter measured at a surface-brightness level of $\mu_B = 25$ mag arcsec^{-2}. Col. (5): Total observed B-band magnitude. Col. (6): Galactic extinction in B band. Col. (7): Internal extinction due to inclination in B band. Col (8): Absolute magnitude in B band.

2 GALAXY SAMPLE

We increased the sample (hereafter S1) presented by François et al. (2019, hereafter Paper I) and analysed in Paper II with 7 old galaxies (hereafter S2) observed with X-shooter (Prop. Id. 384.B-1029(A), PI: Clemens, M. S.) with the same instrumental configuration of the S1 sample. These elliptical galaxies were characterized as passive by Rampazzo et al. (2013). To fill the young stellar population regime, we selected a sample of 11 S0 galaxies (hereafter S3) from the ATLAS 3D survey (Cappellari et al. 2011), with age $1.1 < T < 5.19$ Gyr and metallicity $−0.7 < [Z/H] < 0.40$ dex. Medium-resolution spectroscopy was performed with the UVB ($R \sim 4000$), VIS ($R \sim 5400$), and NIR ($R \sim 4300$) arms of the ESO X-shooter spectrograph (Prop. Id. 106.21CT.001, PI: Gasparri, D.).

In the rest of the paper, we will consider as final sample the combination of the S1, S2, S3 samples. Our final sample is therefore composed by 32 galaxies including 10 ellipticals, 14 S0s, and 8 spirals, roughly uniformly distributed in the velocity dispersion range 30 km s$^{-1} \leq \sigma \leq 335$ km s^{-1} and age range 0.6 Gyr $\leq T \leq 15$ Gyr. The metallicity range is $−0.70 \leq [Z/H] \leq 0.55$ dex, with the bulk of the sample within solar to supersolar values ($−0.30 \leq [Z/H] \leq 0.4$ dex). The mean S/N is ~ 80 pix^{-1} for the UVB arm, ~ 95 pix^{-1} for the VIS arm, and ~ 100 pix^{-1} for the NIR arm. The minimum S/N in the UVB and VIS arms is ~ 20 pix^{-1}, and $\lesssim 10$ pix^{-1} in the NIR arm. Taking into account the S/N, the spectral resolution, and wavelength range of the spectra, along with the sampling of the Hubble type, age, velocity dispersion, and metallicity of the galaxies, our data set is an unparalleled step forward in data quality, compared to prior studies. It serves as an important resource for investigating stellar populations in the NIR bands for local galaxies.

The main properties of the sample galaxies are listed in Table 1 and the distribution of their ages, metallicities, velocity dispersions, and redshifts are shown in Fig. 1.

3 DATA REDUCTION AND ANALYSIS

3.1 Data reduction

The spectra of the galaxies for the S2 and S3 samples have been reduced and analysed following the same procedure of Paper I and Paper II. We resume, here, the steps performed.

For all the targets, multiple exposures have been acquired (for S3 sample) or are available (for the S2 sample) to better remove the detectors' cosmetics and to perform internal consistency of the galaxy spectra.
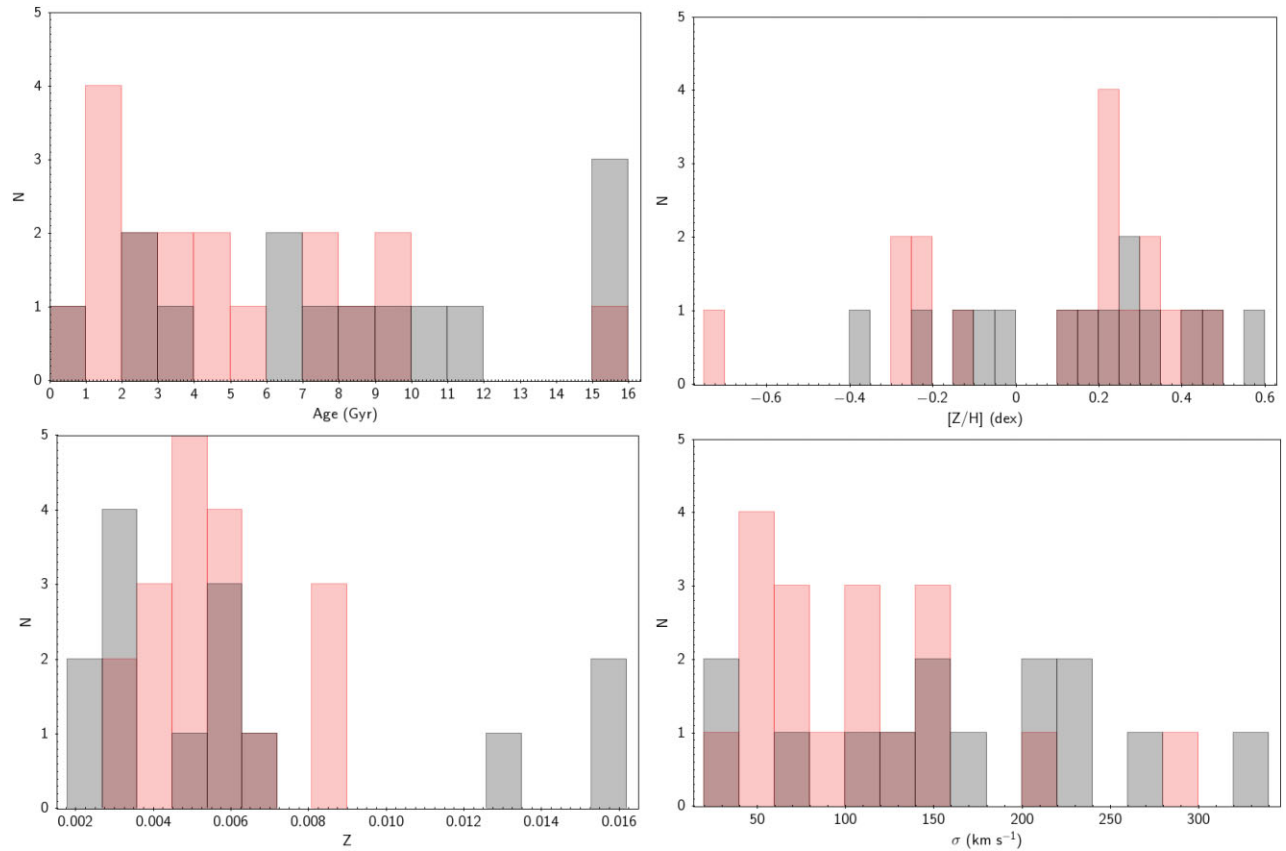
Figure 1. Distribution of age (upper left-hand panel), metallicity (upper right-hand panel), redshift (lower left-hand panel), and velocity dispersion (lower right-hand panel) of the S1 galaxies presented in Paper II (grey) and S2 + S3 galaxies added in this paper (red). The bin size for the age and metallicity matches their mean uncertainties.

The spectra were reduced with the ESO Reflex environment (Freudling et al. 2013) with the X-shooter recipe (Goldoni et al. 2006). The basic processing steps were bias and background subtraction, cosmic ray removal, sky subtraction, flat-fielding, order extraction, and merging. The telluric corrections was performed with the Molecfit software (Smette et al. 2015). As for the S1 sample, for S2 and S3 samples, the spectra were obtained along the major axis of the galaxies and were co-added along the spatial direction to map a central region of 1.5×1.5 arcsec^2, which corresponds to an area ranging from 65×65 to 430×430 pc^2, depending on distance, with a typical S/N ~ 100 pix^{-1}. We performed a cleaning of the residual peaks (3σ) in the 1D spectra generated by cosmic rays and/or imperfect sky subtraction. Similarly to Paper I, to evaluate the internal consistency of the new galaxy spectra, we compared those generated from different observations of the same galaxy, and we found that the root mean square (rms) of the difference over intervals of 15 nm is at 3–5 per cent level, consistent with the results obtained in Paper I for the S1 sample. The telluric correction with Molecfit yielded on average good results, although for some galaxies it produced an overcorrection. We therefore considered only NIR indices not directly affected by strong telluric contamination for our sample galaxies. Figs A1, A2, A3, A4, A5, A6, A7 show the NIR portion of the spectra of the whole sample. The vertical red lines correspond to the central wavelengths of the NIR indices studied in detail in the paper and used to define new age and metallicity indicators.

3.2 Data analysis

We considered, along with the galaxy sample, two semi-empirical models to compare with the data: the EMILES (Röck et al. 2015, 2016; Vazdekis et al. 2016), selected with the BasTI isochrones (Pietrinferni, Cassisi & Salaris 2004), which are considered to give the best results in NIR with respect to other models (Baldwin et al. 2018), and the new and still not well tested XSL models (Verro et al. 2022b). We considered, for both models, the Kroupa IMF (Kroupa 2001).

For the galaxies, we measured the radial velocity and velocity dispersion of the stellar components using a modified version of the penalized pixel fitting (ppxf; Cappellari & Emsellem 2004) and gas and absorption line fitting (GANDALF; Sarzi et al. 2006) code for X-shooter. We also fitted the ionized-gas emission lines in the optical and NIR having a S/N > 3 per spectral element. Finally, the spectra have been corrected to the rest frame. Therefore, for each galaxy and model spectra, we measured the equivalent width (EW) in optical and in the NIR for a sample of 39 indices defined by Cesetti et al. (2013) and Morelli et al. (2020), many of them also measured in Paper II for the S1 sample. The measurements were performed under the IDL environment using a dedicate routine employed also in Paper II, Cesetti et al. (2013); Morelli et al. (2020). The EW was measured directly on the observed spectra. Table B1 shows the definitions of the NIR indices measured in this work.

For the optical atmospheric window, we convolved the spectra (both models and data) to a resolution of FWHM = 8.4 Å to match

Table 2. Central values of velocity dispersion, Lick/IDS line-strength indices, age, and metallicity of the sample galaxies.

Galaxy ID	σ [km s^{-1}]	$\langle$Fe$\rangle$ [Å]	[MgFe]$'$ [Å]	Mg2 [mag]	Mgb [Å]	Hβ [Å]	T [Gyr]	[Z/H] [dex]
NGC 0584	203.9 ± 4.9	3.007 ± 0.143	3.700 ± 0.032	0.283 ± 0.009	4.488 ± 0.145	1.698 ± 0.335	10.1 ± 0.8	0.24 ± 0.02
NGC 0636	169.3 ± 3.8	3.022 ± 0.114	3.684 ± 0.021	0.283 ± 0.004	4.428 ± 0.128	1.798 ± 0.243	7.7 ± 0.8	0.32 ± 0.05
NGC 0897	225.1 ± 1.2	2.788 ± 0.125	3.695 ± 0.023	0.291 ± 0.009	4.809 ± 0.183	1.289 ± 0.141	15.0 ± 1.0	-0.06 ± 0.02
NGC 1357	139.7 ± 2.7	2.814 ± 0.138	3.528 ± 0.037	0.267 ± 0.005	4.348 ± 0.163	1.907 ± 0.241	6.2 ± 0.8	0.29 ± 0.03
NGC 1425	109.6 ± 5.4	2.642 ± 0.142	3.116 ± 0.028	0.215 ± 0.006	3.598 ± 0.192	1.799 ± 0.029	9.6 ± 0.6	-0.01 ± 0.02
NGC 1600	335.1 ± 16.4	2.852 ± 0.137	3.772 ± 0.007	0.306 ± 0.003	4.912 ± 0.245	1.504 ± 0.151	15.0 ± 1.8	0.12 ± 0.04
NGC 1700	226.7 ± 4.2	2.983 ± 0.148	3.630 ± 0.016	0.253 ± 0.005	4.328 ± 0.161	2.183 ± 0.139	2.7 ± 0.2	0.55 ± 0.03
NGC 2613	152.0 ± 5.9	2.836 ± 0.156	3.496 ± 0.018	0.260 ± 0.002	4.231 ± 0.143	1.888 ± 0.140	6.5 ± 0.7	0.27 ± 0.02
NGC 3115	274.8 ± 3.2	3.284 ± 0.146	4.101 ± 0.025	0.323 ± 0.009	5.029 ± 0.200	1.682 ± 0.144	8.0 ± 1.1	0.47 ± 0.03
NGC 3377	153.4 ± 4.6	2.792 ± 0.098	3.512 ± 0.018	0.243 ± 0.008	4.329 ± 0.230	2.119 ± 0.129	3.5 ± 0.1	0.43 ± 0.01
NGC 3379	219.8 ± 3.2	2.970 ± 0.133	3.876 ± 0.027	0.318 ± 0.002	4.968 ± 0.187	1.488 ± 0.150	15.0 ± 1.7	0.15 ± 0.04
NGC 3423	38.2 ± 5.5	2.111 ± 0.125	2.159 ± 0.022	0.119 ± 0.004	2.094 ± 0.127	2.758 ± 0.148	2.2 ± 0.6	-0.15 ± 0.07
NGC 4415	35.9 ± 2.6	1.987 ± 0.243	2.406 ± 0.018	0.169 ± 0.006	2.821 ± 0.169	1.865 ± 0.178	11.4 ± 4.6	-0.39 ± 0.15
NGC 7424	60.8 ± 1.4	1.483 ± 0.305	1.461 ± 0.015	0.081 ± 0.007	1.383 ± 0.086	4.422 ± 0.166	0.8 ± 0.8	-0.22 ± 0.05
NGC 7465	99.8 ± 4.0	1.889 ± 0.068	1.946 ± 0.077	0.114 ± 0.021	1.982 ± 0.090	2.946 ± 0.060	2.0 ± 0.2	-0.26 ± 0.10
IC 0676	48.4 ± 4.5	1.611 ± 0.061	1.656 ± 0.051	0.077 ± 0.010	1.759 ± 0.065	2.699 ± 0.106	4.9 ± 0.2	-0.72 ± 0.08
NGC 0516	44.9 ± 5.0	2.067 ± 0.103	2.265 ± 0.101	0.162 ± 0.008	2.350 ± 0.089	2.399 ± 0.076	4.1 ± 0.8	-0.23 ± 0.05
NGC 4124	38.1 ± 5.4	2.180 ± 0.084	2.284 ± 0.082	0.151 ± 0.007	2.365 ± 0.072	3.415 ± 0.074	1.1 ± 0.3	0.21 ± 0.05
NGC 4324	71.4 ± 4.1	2.882 ± 0.105	3.266 ± 0.099	0.239 ± 0.006	3.651 ± 0.087	2.335 ± 0.056	2.3 ± 1.0	0.45 ± 0.05
NGC 4643	150.5 ± 4.6	2.417 ± 0.086	2.824 ± 0.086	0.245 ± 0.005	3.311 ± 0.090	1.904 ± 0.071	9.5 ± 1.1	-0.14 ± 0.05
NGC 4684	75.1 ± 4.1	2.144 ± 0.071	2.395 ± 0.081	0.123 ± 0.034	2.899 ± 0.091	2.265 ± 0.083	5.1 ± 0.7	-0.21 ± 0.08
NGC 5574	50.1 ± 4.0	2.225 ± 0.096	2.449 ± 0.077	0.168 ± 0.007	2.638 ± 0.076	3.195 ± 0.042	1.3 ± 0.2	0.24 ± 0.06
NGC 5854	105.6 ± 4.0	2.531 ± 0.086	2.719 ± 0.071	0.185 ± 0.007	2.897 ± 0.060	2.694 ± 0.038	1.8 ± 0.3	0.24 ± 0.05
NGC 7693	51.5 ± 6.6	1.679 ± 0.077	1.751 ± 0.061	0.102 ± 0.010	1.748 ± 0.058	4.684 ± 0.073	0.6 ± 0.1	0.22 ± 0.06
PGC 56772	77.0 ± 3.9	1.868 ± 0.064	2.040 ± 0.068	0.109 ± 0.011	2.282 ± 0.078	2.692 ± 0.089	2.3 ± 0.4	-0.29 ± 0.06
NGC 1389	119.2 ± 5.5	2.917 ± 0.106	3.487 ± 0.113	0.267 ± 0.005	4.112 ± 0.086	2.105 ± 0.050	3.5 ± 0.7	0.43 ± 0.01
NGC 1426	152.5 ± 7.5	3.032 ± 0.097	3.729 ± 0.091	0.292 ± 0.005	4.514 ± 0.079	1.779 ± 0.045	8.0 ± 1.9	0.33 ± 0.01
NGC 3818	200.0 ± 5.5	2.851 ± 0.070	3.873 ± 0.076	0.320 ± 0.004	5.169 ± 0.055	1.388 ± 0.032	15.3 ± 1.2	0.10 ± 0.01
NGC 4339	121.1 ± 5.7	3.010 ± 0.108	3.519 ± 0.100	0.265 ± 0.005	4.018 ± 0.078	1.815 ± 0.048	7.4 ± 1.7	0.25 ± 0.05
NGC 4365	283.3 ± 4.6	3.141 ± 0.071	3.914 ± 0.066	0.318 ± 0.004	4.910 ± 0.044	1.712 ± 0.018	9.1 ± 2.0	0.37 ± 0.05
NGC 4371	117.2 ± 9.0	2.862 ± 0.103	3.277 ± 0.101	0.254 ± 0.006	3.623 ± 0.106	2.088 ± 0.046	4.0 ± 0.7	0.31 ± 0.05
NGC 4377	146.6 ± 6.7	2.776 ± 0.087	3.378 ± 0.076	0.257 ± 0.005	4.023 ± 0.081	1.854 ± 0.035	7.7 ± 1.2	0.17 ± 0.05

that of the Lick/IDS system in the 0.40–0.54 μm range. We measured 19 Lick/IDS indices (Faber et al. 1985; Worthey et al. 1994), including the Mg, Fe, Hβ, $\langle$Fe$\rangle$ mean index (Gorgas, Efstathiou & Aragon Salamanca 1990) and the [MgFe]$'$ combined index (Thomas et al. 2003), which are used as stellar population indicators. Velocity dispersion corrections and the total error estimation for the galaxy sample have been performed following Trager et al. (1998). We derived the stellar population properties of the sample galaxies using the SSP models by Johansson et al. (2010). The models predict the values of the line-strength indices for a single stellar population as a function of age, metallicity, and [α/Fe] ratio. The selection of these models was made to ensure consistency with the results obtained in Paper I and Paper II on the S1 sample, but is not crucial for the results presented in this paper. In this study, indeed, we have focused on finding new stellar populations indicators in the NIR through direct correlations with the population diagnostics in the optical atmospheric window.

The central mean age and total metallicity of the stellar populations of the sample galaxies were derived from the values of line-strength indices Hβ and [MgFe]$'$ by a linear interpolation between the model points using an iterative routine in IDL described in Morelli et al. (2004, 2008, 2016). The uncertainties in ages and metallicities have been estimated with MonteCarlo simulations. Typical uncertainties for age are ∼0.7 Gyr and ∼0.05 dex for metallicity. The Lick/IDS indices used as stellar diagnostics, velocity dispersion, and derived properties of the stellar populations for all the galaxies

with the relative uncertainties of the final sample are listed in Table 2.

For the NIR, we reduced the resolution of the galaxy spectra and XSL models to match that of the EMILES models in NIR ($R = 2000$), and we resampled the spectra to the common linear step $\Delta\lambda = 1$ Å in order to have consistent measurements. We corrected the measured EWs of the indices of galaxies to zero velocity dispersion following the method of Silva et al. (2008) and Cesetti et al. (2009) by broadening a sample of K and early M stars of the IRTF spectral library up to 400 km s^{-1} and calculating the spline coefficients of the mean EW values as a function of the velocity dispersion. For the total error estimation, we also considered the uncertainties associated to the correction coefficients, which we added in quadrature to the intrinsic errors. The EWs of the 39 NIR indices for all the galaxies are reported in Tables B2, B3, and B4.

4 NEW NIR INDICES AS GALAXY AGE AND METALLICITY DIAGNOSTICS

In Paper II, to investigate the possible use of the NIR indices as age and metallicity indicators, we compared some of them with a set of optical indices known to be the best diagnostics of stellar population properties. We used the Hβ index as an age indicator, the $\langle$Fe$\rangle$, Mg2, Mgb, and [MgFe]$'$ indices as metallicity tracers. We found some strong correlations, as for example, Paβ-Hβ or [AlFeH]-Mg2. To further explore this idea, we started the work presented in this paper
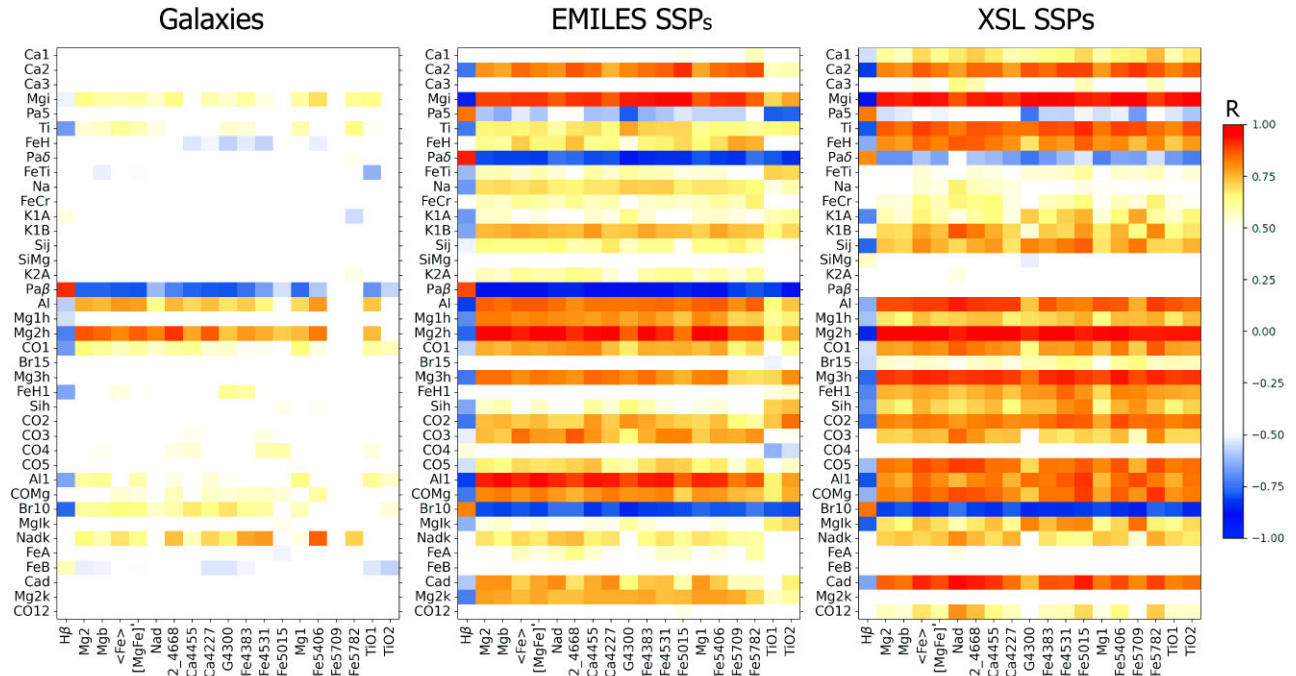
Figure 2. Correlation matrix for the 39 NIR indices with Lick/IDS indices for a subsample of galaxies with [Z/H] < 0.25 (left-hand panel) and corresponding EMILES (middle panel) and XSL (right-hand panel) SSP models. Different colours correspond to different degrees of correlation according to Pearson statistics. For sake of clarity, only moderate-to-strong correlations (Pearson coefficient $|R| > 0.5$) are shown.

by analysing the connections between the 19 Lick/IDS indices and the 39 NIR indices.

To this aim, we calculated the correlation matrix between the NIR and Lick/IDS indices for the galaxies (Fig. 2, left-hand plot). We limited our galaxy sample to [Z/H] < 0.25 dex in order to make comparisons within the safe zone of both the considered models. We also added the ⟨Fe⟩ and [MgFe]′ indices. The EW of the two CN, Hδ, and Hγ Lick/IDS indices could not be measured due to the low S/N.

In Fig. 2 only moderate-to-strong correlations are shown (Pearson coefficient $|R| > 0.5$). We found that eight NIR indices, namely the Ti, Paβ, Al, Mg2h, CO1, Al1, FeH1, and Nadk show strong or moderate correlations with several Lick/IDS indices for the sample galaxies (left-hand panel). In particular, the Paβ, Al, Al1, Mg2h, CO1, and FeH1 show clear trends with the optical Hβ index (Paper II, Eftekhari, Vazdekis & La Barbera 2021).

In the middle and right-hand panels of Fig. 2, we plotted the same correlation matrix for the EMILES and XSL models, with a Kroupa IMF, matching the age and metallicity of the sample galaxies. The distribution of the Pearson coefficients in the correlation matrix of the two models is similar. They agree with each other for all the indices, except for the Paβ.

As a general result, we found that the distribution of the Pearson coefficients in the correlation matrix of the indices measured for galaxies is consistent with the correlation matrix of the indices measured for models, theoretically confirming the empirical correlations we found. There are only few exception: i) The Cad index, whereas it correlates consistently in both models with the Hβ, does not correlate with the observational data. This is due to a large scatter in its EW by the low S/N and residual telluric contamination in the index definition bands; ii) The Br10 index for galaxies shows inverted correlations with respect to the models, likely due to residual telluric contamination.

4.1 NIR composite indices as metallicity indicators

In order to maximize the correlations between the NIR indices and the Lick/IDS indices used as age, metallicity, and α-element enhancement diagnostics, we compared particular combinations of the NIR indices with the Mg2, Mgb, ⟨Fe⟩, and [MgFe]′ indices, starting from the correlations of Fig. 2 for the galaxy sample. We then compared the results with the predictions of EMILES models selected within $-0.66 <$ [Z/H] < 0.26 dex, 0.8 Gyr $< T < 14$ Gyr, and the XSL models, selected within $-0.6 <$ [Z/H] < 0.2 dex, 0.8 Gyr $< T < 15$ Gyr, both with Kroupa IMF.

We started our analysis from the two Al indices (Al and Al1), since they are relatively strong (⟨EW⟩ > 1 Å) and show a good correlation with the Lick/IDS indices. Furthermore, they are not blended with other metallicity indices and reside in a wavelength range devoid of strong atmospheric lines for local galaxies (Figs A1, A2, A3, A4, A5, A6, and A7). We defined the first composite index as:

$$Al^* = Al + 0.5Al1, \qquad (1)$$

where the coefficients have been empirically determined to maximize the correlations with the Lick/IDS metallicity diagnostics. In the upper panel of Fig. 3, we present the correlations of the Al* with the Mg2, Mgb, ⟨Fe⟩, and [MgFe]′ indices for the sample galaxies. Different symbols denote different morphological types and their size is proportional to the measured velocity dispersion. We overplotted also the EMILES (grey dots) and XSL (orange dots) model predictions. In the second panel of Fig. 3, we included the [AlFeH] composite index defined in Paper II. The uncertainties of the Pearson coefficients in this and the following figures have been estimated with the bootstrapping statistical procedure, by creating 10 000 simulated samples for each correlation.

The NIR Al* index has the largest value of Pearson coefficient in the correlations with the two Mg indices. A slightly large scattering is observed with the ⟨Fe⟩ index, which shows the smallest
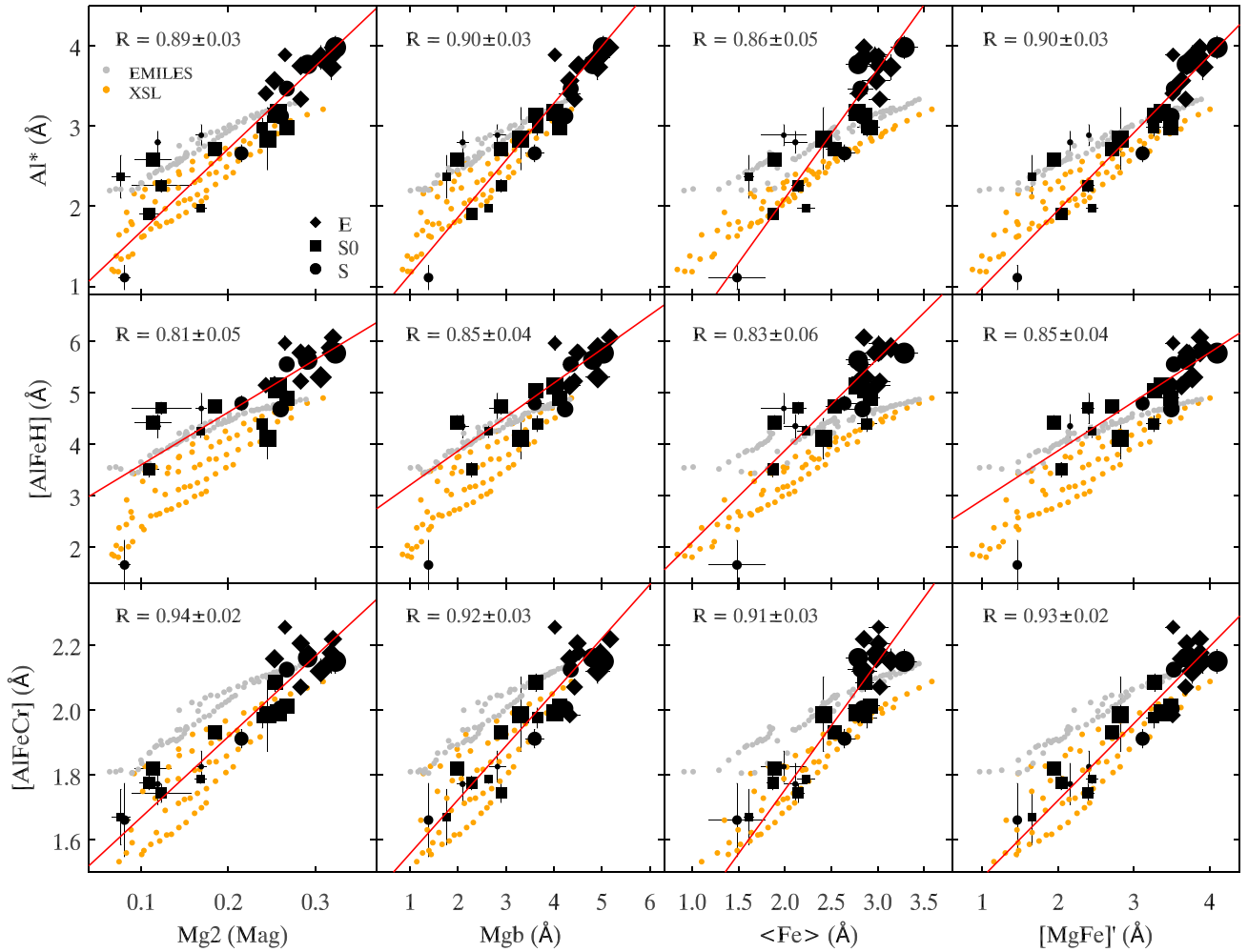
Figure 3. Correlations for the composite NIR indices with Lick/IDS indices used as stellar population diagnostics. The small grey dots represent the EMILES models. The small orange dots are the XSL models. The galaxies are the larger data points with error bars. Different symbols denote the three morphological classes: ellipticals (E, diamonds), S0 (squares), and spirals (S, circles). The symbol size is proportional to the velocity dispersion. The red line is the best linear fit considering errors in both axes. The Pearson correlation coefficient (*R*) and the associated uncertainty estimated with bootstrap simulations is shown for every plot.

Pearson coefficients of the series. Therefore, in our sample, we found that Al is more sensitive to α-elements rather than the iron content, confirming the findings of Bensby, Feltzing & Oey (2014) who identified aluminum as a good α-element tracer for the Milky Way and theoretically supported by Pignatari et al. (2016), who suggested a shared formation processes of the Mg, Si, and the Al.

To improve the correlation with the $\langle$Fe$\rangle$ index and the optical metallicity indicator [MgFe]′, we tried to add to the Al* an iron index, not contaminated by telluric absorption or blended with other spectral lines. We found that the best result is achieved with the following composite index:

$$[AlFeCr] = \sqrt{Al^* + 1.4FeCr}, \tag{2}$$

where the coefficients have been determined to maximize the correlation with the [MgFe]′ index.

The addition of the FeCr index ($\lambda \sim 1.16\,\mu m$) to Al* to form the [AlFeCr] combined index improves the Pearson coefficient in the correlations with all the optical metallicity indices (Fig. 3, lower panel), particularly with the $\langle$Fe$\rangle$ and [MgFe]′. This indicates that the

FeCr index drives the sensitivity of [AlFeCr] toward the total metal content. Both the Al* and the [AlFeCr] indices improve the [AlFeH] index defined in Paper II.

None of the relations in Fig. 3 shows any clear effect related with the morphological types of the galaxies and/or with their velocity dispersion. The models successfully replicate all the observed correlations and exhibit a significant overlap with the data, particularly in the case of the XSL.

Due to the high degree of correlations between the here defined NIR composite indices and Lick/IDS indices used as stellar population indicators, we derived empirical calibration equations. The best-fitting relationships between the Lick/IDS metallicity indicators and Al* and [AlFeCr] composite indices are the following:

$$Mg_2\,(mag) = (0.097 \pm 0.003)Al^* \\ + (-0.064 \pm 0.010)\,rms = 0.036\,(mag) \tag{3}$$

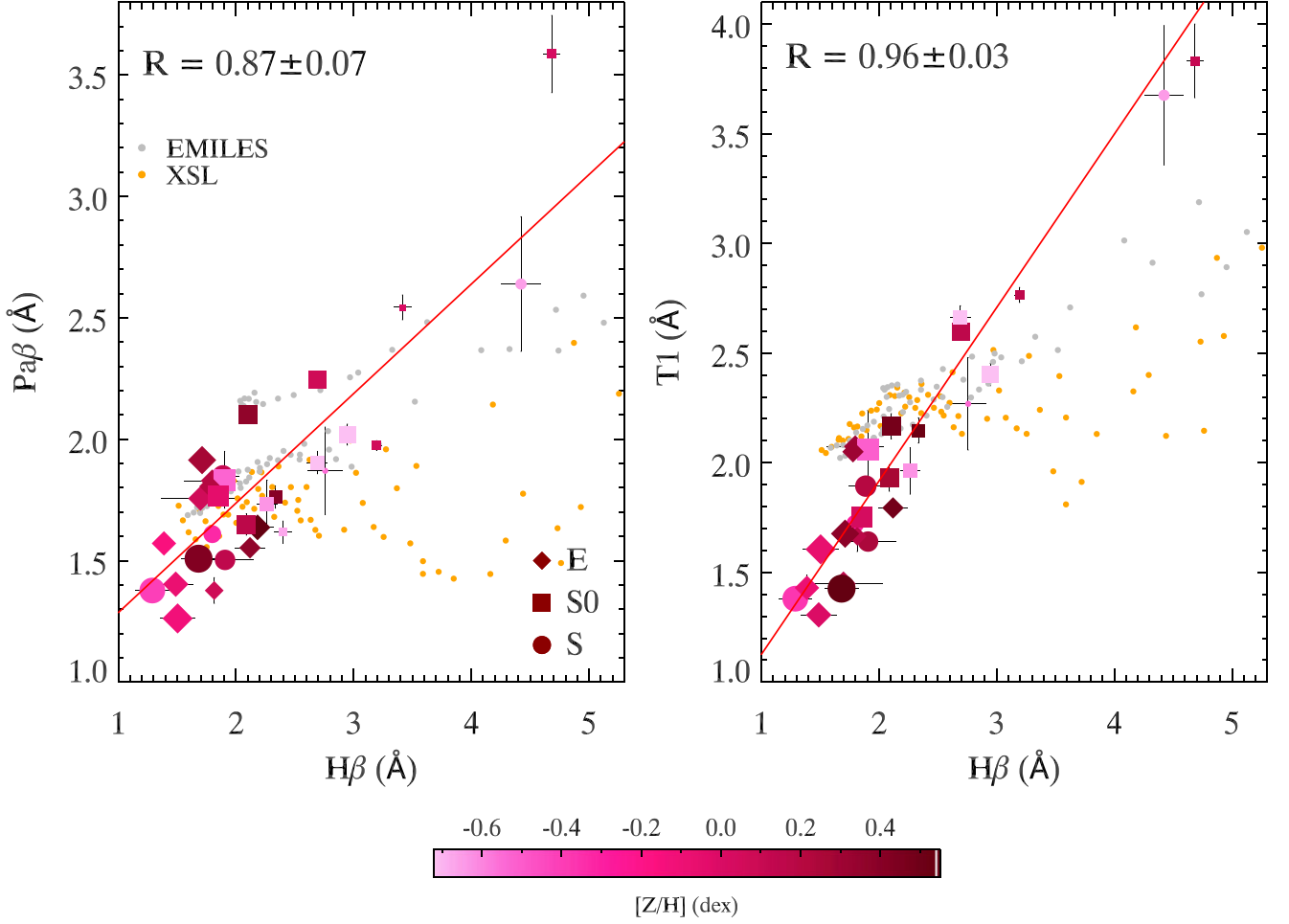$$Mg_b\,(\text{Å}) = (1.405 \pm 0.043)Al^* \\ + (-0.617 \pm 0.137)\,rms = 0.470\,(\text{Å}) \tag{4}$$

Figure 4. Correlations between the Paβ and Hβ indices (left-hand panel) and between the T1 composite index and Hβ (right-hand panel). The small grey dots represent the EMILES models. The small orange dots are the XSL models. The galaxies are the larger data points with error bars, colour coded following the metallicity. Different symbols denote the three morphological classes: ellipticals (E, diamonds), S0 (squares) and spirals (S, circles). Symbol size is proportional to the velocity dispersion. The red line is the best linear fit considering errors in both axis. The Pearson correlation coefficient (*R*) and the associated uncertainty estimated with bootstrap simulations is shown for every plot.

$$\mathrm{Mg}_2\,(\mathrm{mag}) = (0.402 \pm 0.017)[\mathrm{AlFeCr}]$$
$$+ (-0.571 \pm 0.034)\,\mathrm{rms} = 0.026\,(\mathrm{mag}) \quad (5)$$

$$\mathrm{Mg}_b\,(\text{Å}) = (6.035 \pm 0.225)[\mathrm{AlFeCr}]$$
$$+ (-8.401 \pm 0.451)\,\mathrm{rms} = 0.441\,(\text{Å}) \quad (6)$$

$$\langle\mathrm{Fe}\rangle\,(\text{Å}) = (2.537 \pm 0.140)[\mathrm{AlFeCr}]$$
$$+ (-2.450 \pm 0.280)\,\mathrm{rms} = 0.197\,(\text{Å}) \quad (7)$$

$$[\mathrm{MgFe}]'\,(\text{Å}) = (4.225 \pm 0.160)[\mathrm{AlFeCr}]$$
$$+ (-5.273 \pm 0.320)\,\mathrm{rms} = 0.273\,(\text{Å}). \quad (8)$$

The equations and the uncertainties of the parameters have been computed with the FITEXY procedure contained in the IDL Astronomy Users Library (Landsman 1995). The typical fractional uncertainties associated to the empirical calibration equations are approximately 10 per cent for intermediate-to-old and 20 per cent for young stellar populations (*T* < 2 Gyr).

4.2 NIR composite indices as age indicators

Following the same strategy used for the metallicity, we repeated the same analysis focusing to possible age indicators of the stellar populations.

In Paper II, we found that the Paβ index is the sole strong and not contaminated hydrogen index to tightly correlate with the Hβ index. In the left-hand panel of Fig. 4, we present the updated Paβ-Hβ relation for our larger sample of galaxies and confirm the correlation between the two indices thanks to the addition of the young stellar-population (Hβ > 2 Å) galaxies of our S3 sample. In the figure, we observe some scatter in the correlation that could be due to metallicity contamination: subsolar metallicity galaxies tend to lie below the best-fitting line, while the high-metallicity galaxies tend to lie above the line, for Hβ > 2 Å.

In order to test the dependency from the metallicity, reduce the scatter and tighten the correlation with the *Hβ* index, we tried to combine the Paβ index with other relatively strong atomic metal indices. We found that the best result is reached by the following composite index:

$$\mathrm{T1} = \mathrm{Pa}\beta + 0.3\mathrm{CaT} - 0.5\mathrm{Sih} - 0.2\mathrm{Al}, \quad (9)$$
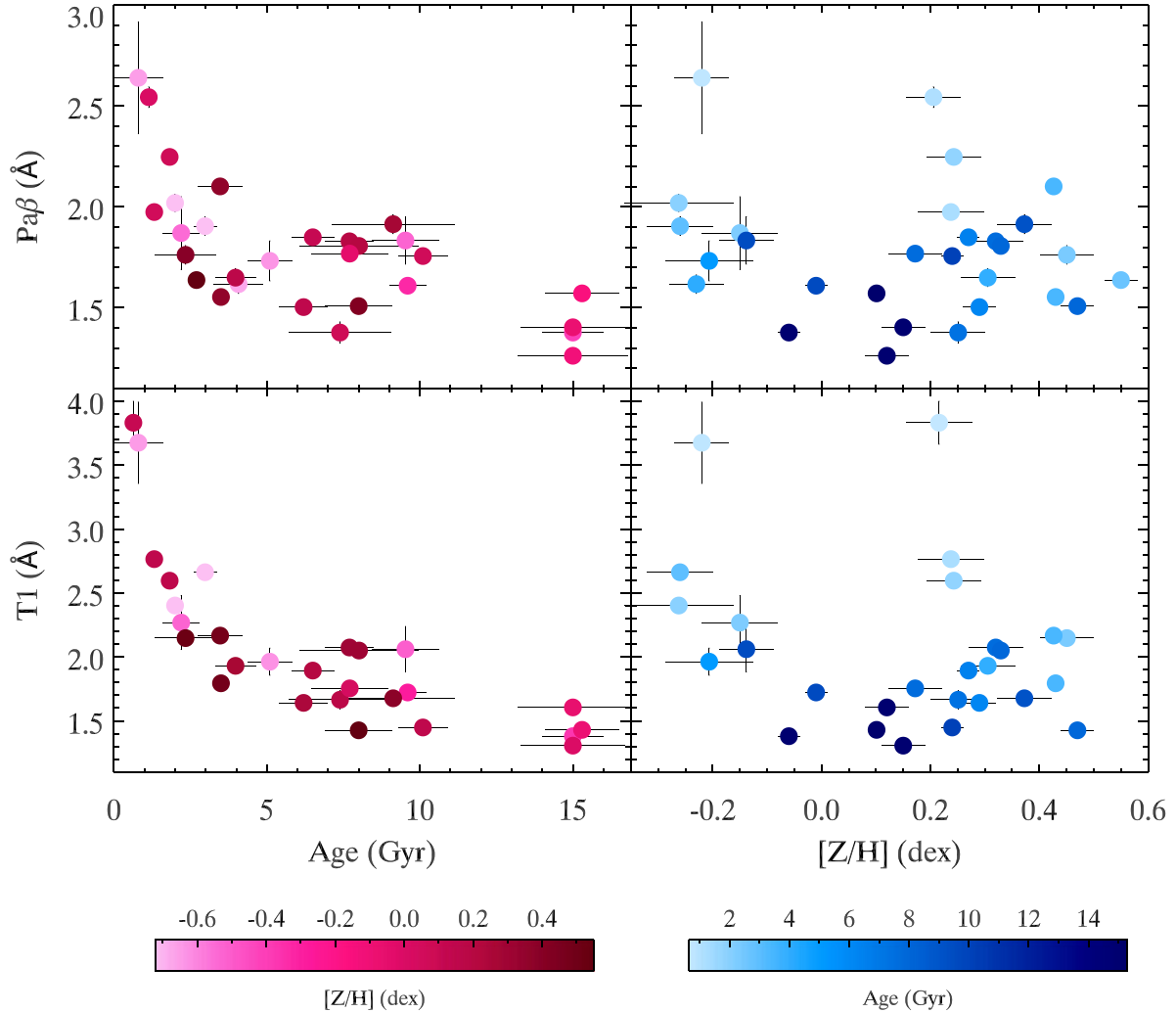
Figure 5. NIR Paβ (upper panels) and T1 (lower panels) indices versus age (left-hand panels) and metallicity (right-hand panels) obtained using the stellar populations models of Johansson et al. (2010) in the optical range. Data points are colour coded from low (brighter hues) to high (darker hues) metallicity in the right-hand panels and from young (brighter hues) to old (darker hues) age, in the left-hand panels.

where the coefficients for the CaT, Sih ($\lambda \sim 1.59\,\mu$m) and Al have been empirically determined to maximize the correlation with the Hβ index.

The T1–Hβ correlation is shown in the right-hand panel of Fig. 4. We see a substantial improvement of the Pearson correlation coefficient, from $R = 0.87$ to 0.96, with a noticeably reduced scatter. The T1 index variation with age is slightly shallower with respect to the Hβ index, but it is still much larger than the average uncertainties in the index measurements (~ 30 times).

In both plots, we do not observe any effect due to different morphological types and/or velocity dispersion. The models (grey dots for EMILES and orange dots for XSL) do not reproduce well the trends both for the Paβ and the T1. The EMILES and XSL overestimate the Paβ and the T1 for low values of Hβ (i.e. old stellar populations) and underestimate them for high values of Hβ (i.e. young stellar populations). For Hβ $\gtrsim 3$, the two models exhibit very distinct behaviours.

Considering the high degree of correlation between the here defined T1 composite index and the Lick/IDS Hβ age indicator, we derived the empirical calibration equation. The best fit relationship

is the following:

$$\text{H}\beta\,(\text{Å}) = (1.244 \pm 0.040)\text{T1}$$
$$+ (-0.394 \pm 0.083)\,\text{rms} = 0.219\,(\text{Å}). \tag{10}$$

The typical fractional uncertainties associated to the empirical calibration equation are approximately 15 per cent for old (Hβ < 2.2 Å) and 10 per cent for intermediate-to-young stellar populations.

5 COMPARISON OF THE NEW NIR INDICES WITH STELLAR PARAMETERS AND STELLAR POPULATION MODELS

The Paβ index and the new NIR indices Al*, [AlFeCr], and T1 defined in Section 4 have very strong correlations with the Lick/IDS indices used as age and metallicity diagnostics. In this section, we compared these indices directly with age and metallicity values derived from the Lick/IDS line-strength analysis and showed in Table 2. Then, we compared the EW of these new NIR indices with the predictions of the EMILES and XSL models.
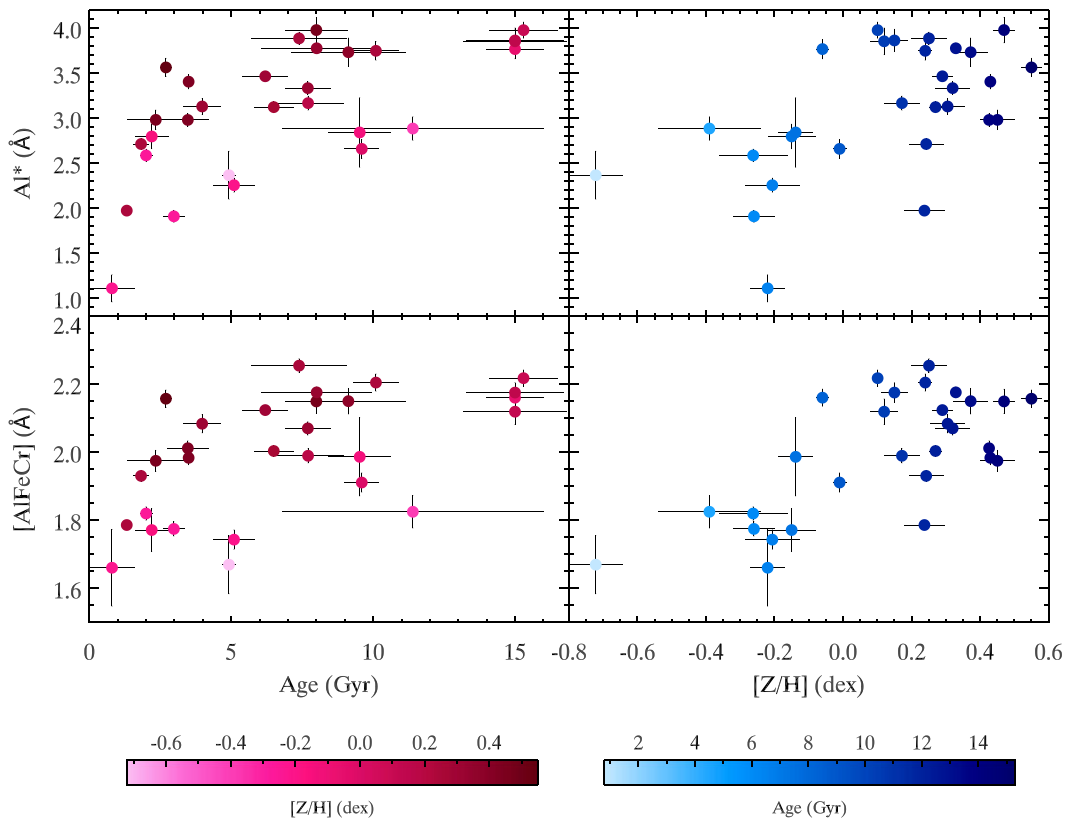
Figure 6. Same as in Fig. 5 but for the Al* and [AlFeCr] composite indices.

5.1 Comparison with the optical age and metallicity

The two candidates as age indicators in NIR are the Paβ index and the T1 composite index. In the upper panel of Fig. 5, we compared the trend of the Paβ index with the mean age (left-hand panel) and metallicity (right-hand panel) of the stellar populations of the sample galaxies. The correlation with age has a moderate scatter, which tends to increase for galaxies older than 6 Gyr (Fig. 5, upper-left-hand panel), making the relation to degenerate. The correlation with metallicity (upper-right-hand panel) is flat with a large scatter.

In the lower panel of Fig. 5, we compared the trend of the T1 composite index with the mean age (left-hand panel) and metallicity (right-hand panel) of the stellar populations of the sample galaxies. The correlation with age has a scatter smaller than the Paβ index. That makes the T1 index more reliable for a larger range of ages, at least up to 10–12 Gyr (Fig. 5, lower-left-hand panel). The distribution with metallicity (lower-right-hand panel) has a lower scatter than the Paβ index and no clear trends. Considering also the very tight correlation with Hβ, this result confirms that the T1 index is the most promising age indicator in NIR.

In Fig. 6, we present the trend of Al* and [AlFeCr], proposed as metallicity tracers, with the mean age (left-hand panel) and metallicity (right-hand panel) of the stellar populations of the sample galaxies.

Both the two composite indices display a good sensitivity to the metallicity and the moderate scatter make them a good candidates for deriving the stellar component metallicity in the NIR wavelength range.

From the correlation of Al* and the [AlFeCr] composite indices with age, it is possible to note a moderate dependence of these indices

with age. This is probably due to their constructions, since [MgFe]$'$ shows similar dependence for young ages galaxies.

To conclude this section, it is worth mentioning that although attempts were made to find better composite indices as indicators of [α/Fe], it was not possible to identify any better than the <Al> proposed in Gasparri et al. (2021) or the Al* here proposed.

5.2 Comparison with the NIR stellar populations models

In the optical range, comparison between indices and theoretical model predictions to obtain stellar population properties is a widely used diagnostics tool (e.g. Sánchez-Blázquez et al. 2006; Morelli et al. 2008). In this section, we adopted the same approach to test the T1 and [AlFeCr] indices with the NIR model predictions based on the EMILES and XSL libraries.

The diagnostic diagram of the central values of the EW of T1 and [AlFeCr] with the XSL (upper panels) and EMILES (lower panels) model predictions is shown in Fig. 7. We also included, as references, the [MgFe]$'$–Hβ diagnostic diagram obtained with the same models. In this diagram, data are in good agreements with both the models.

In the metal-rich region of the diagrams, observational data are slightly out from the model grids since some of the sample galaxies display a metallicity value larger than the model metallicity range available and/or within their safe zones. The sample galaxies are colour coded according to their mean age and total metallicity, which we derived in Paper II and Section 3.

As general consideration, the distributions of data points in the [AlFeCr]-T1 diagram well match that of the [MgFe]$'$–Hβ diagram. Indeed, the younger and more metal-poor galaxies lie in the upper left region, while the older and more metal-rich galaxies are in the lower
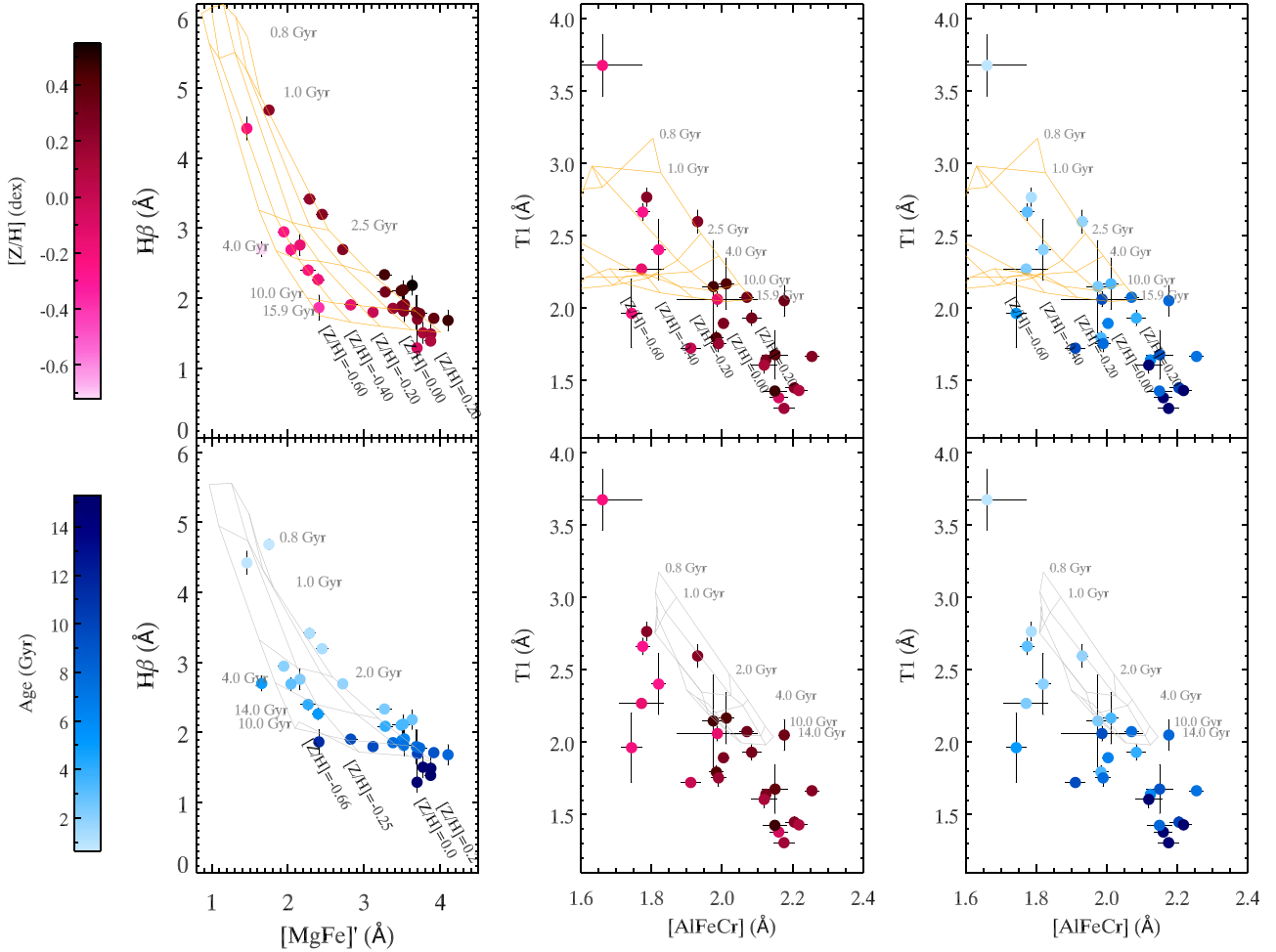
Figure 7. The distribution of the central values of Hβ and [MgFe]′ indices (left-hand panel) and T1 and [AlFeCr] indices (middle and right-hand panel) for the sample galaxies. The lines indicate the XSL models (upper panel, orange lines) and the EMILES models (bottom panel, grey lines). Galaxies are colour coded according to their optically derived age (blue) and metallicity (purple). Darker hues means higher metallicity/older age; brighter hues means lower metallicity/younger age.

right region, indicating that T1 and [AlFeCr] composite indices are effective in discerning age and metallicity, respectively.

The model grids built with T1 and [AlFeCr] indices (Fig. 7, middle and right-hand panels) have only a partial overlap with the data. The metallicity range covered by the models approximately matches the range of the observational data, and the galaxies are well separated in metallicity in the [AlFeCr]-T1 diagram. On the opposite, the situation for the age seems to be more complicated. The vertical extent of the observational data for the T1 composite index is larger than that reproduced by the models in the case of the EMILES (lower panels of Fig. 7), while it seems to be shifted towards higher ages in the case of the XSL (upper panels of Fig. 7).

To better address this issue, we have tried to break the problem into two parts by separating the age from metallicity. To this aim, we made two similar plots substituting the NIR T1 composite index with the optical Hβ index. The result is shown in Fig. 8. In these plots, models and data are matching much better. In the [AlFeCr]–Hβ diagram, the XSL models (upper panel of Fig. 8) are well separated in metallicity for all the Hβ values. The separation is larger than that provided by the [MgFe]′ index for age < 4 Gyr. In the Hβ–[AlFeCr] diagram with the EMILES models (lower panel of Fig. 8), the situation is similar but the models predict a shorter range for

the [AlFeCr] values and make more data points to lie out of the grid.

We conclude that T1 and [AlFeCr] are good age and metallicity tracers. However, some fine tuning of NIR models is still needed to use them for directly deriving age and metallicity via interpolation of the model grids.

6 CORRELATIONS BETWEEN NIR INDICES AND VELOCITY DISPERSION

In the NIR regime, some line-strength indices have been known to have correlations with the velocity dispersion. Cenarro et al. (2003) discovered a strong anticorrelation between the CaT index and velocity dispersion in the central regions of 35 early-type galaxies, which was extended to the bulges of spiral galaxies by Falcón-Barroso et al. (2003). Garcia-Rissmann et al. (2005) studied the CaT lines in active galaxy spectra. Silva et al. (2008), Mármol-Queraltó et al. (2009), Röck et al. (2017) considered also the strong CO bands. The strong CO 2.29 μ band heads have been investigated also by Riffel et al. (2015) and show different values of velocity dispersion with respect to the CaT lines; this has been interpreted as the effect
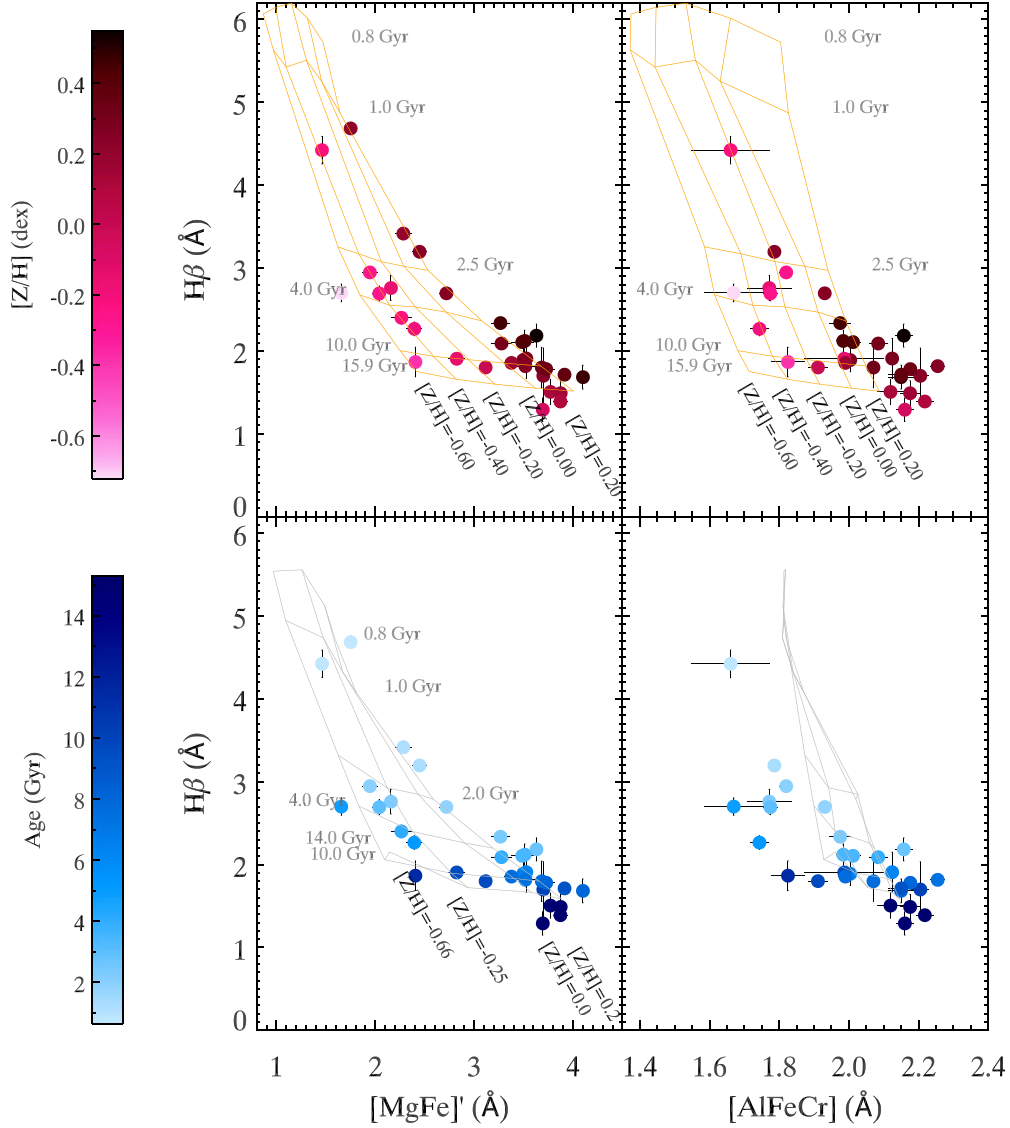
Figure 8. The distribution of the central values of Hβ and [MgFe]′ indices (left-hand panel) and Hβ and [AlFeCr] indices (right-hand panel) for the sample galaxies. The lines indicate the XSL models (upper panel, orange lines) and the EMILES models (bottom panel, grey lines). Galaxies are colour coded according to their optically derived age (blue) and metallicity (purple). Darker hues mean higher metallicity/older age; brighter hues mean lower metallicity/younger age.

of a warm dust component or a dynamically cold stellar population component.

In Paper II, we pointed out that the Al and Al1 indices are tightly correlated with the velocity dispersion, while the Paβ index shows a moderate anticorrelation with it. Here, we extended these finding by looking for a composite index that correlates more effectively with velocity dispersion.

Following the same procedure adopted in Section 4, we found a new correlation between the velocity dispersion and Mg2h (λ ∼ 1.50 μm) index, which is the strongest magnesium index in NIR. The correlation Mg2h–σ is shown in the left-hand panel of Fig. 9. Therefore, we built a new composite index to be more sensitive to velocity dispersion by combining the Al1 index with Mg2h, and normalizing by the CaT index. The result of this exercise is the new Σ1 composite index, defined as:

$$\Sigma 1 = (Mg2h + 1.7Al1)/CaT, \qquad (11)$$

where the coefficient for the Al1 has been empirically determined to maximize the Pearson correlation coefficient of the relation with velocity dispersion ($R = 0.92$). In Fig. 9 (right-hand panel), the Σ1–σ relation is shown. The best fitting relationship between the Σ1 with the velocity dispersion is the following:

$$\log \sigma (\text{km s}^{-1}) = (0.884 \pm 0.033)\Sigma 1$$
$$+ (1.073 \pm 0.040) \, \text{rms} = 0.08. \qquad (12)$$

The final rms scatter is comparable with that of the optical Mg2–σ relation (e.g. Jorgensen 1997).

7 DISCUSSION AND CONCLUSION

We investigated the connection between the EW of 19 Lick/IDS indices and 39 NIR indices defined by Cesetti et al. (2013) and Morelli et al. (2020) and measured in the central regions of 32 galaxies observed with X-shooter from the near UV to NIR (0.3–2.4 μm). We aimed at finding new age and metallicity diagnostics in
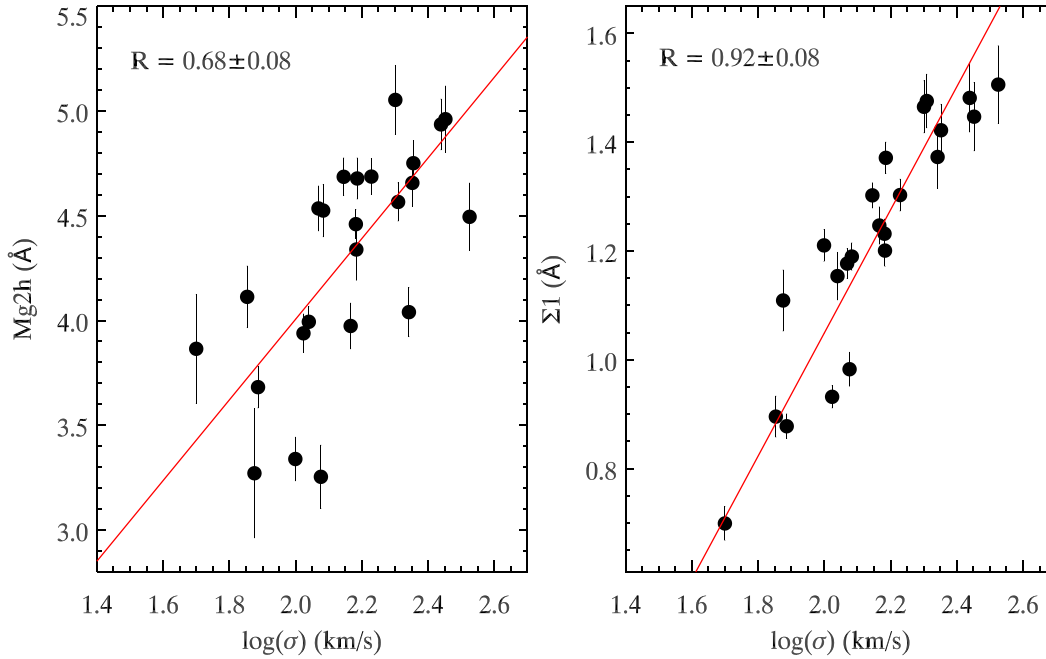
Figure 9. Correlations of the Mg2h (left-hand panel) and Σ1 composite (right-hand panel) index with the central velocity dispersion of the sample galaxies. The best linear fit (red line) is given for each plot. The Pearson correlation coefficients are reported for each correlation.

NIR to investigate the formation and evolution of dust obscured galaxies by measuring the properties of their unresolved stellar populations.

We adopted a systematic approach, deriving first a correlation matrix between all the optical Lick/IDS and NIR indices measured for the galaxies, then building new NIR composite indices to maximize the correlations with the optical age and metallicity indicators.

We found that the NIR Ti, Paβ, Al, Mg2h, CO1, Al1, FeH1, and Nadk indices show a strong or moderate correlation with several Lick/IDS indices. In particular, the Paβ, Al, Al1, Mg2h, CO1, and FeH1 indices show clear trends with the optical Hβ index, confirming the findings of Paper II and Eftekhari et al. (2021).

Of particular interest are the two Al indices, emerging as promising metallicity diagnostics. Despite not being an α-element, Bensby et al. (2014) identified aluminum as a reliable α-element tracer for the Milky Way, while Pignatari et al. (2016) theorized of shared formation processes of Mg, Si, and Al. The correlation with velocity dispersion presented in Paper II, and strong trends with Lick/IDS Mg-based indices Fig. 3 confirmed that the aluminum indices may serve as the most effective α-element proxy in the NIR, providing a solid foundation for constructing a total metallicity indicator when combined with NIR iron-based indices.

The FeCr index may serve as a robust tracer of iron abundance in galaxies in the NIR domain. Pignatari et al. (2016) confirmed that the most abundant and stable isotope of Cr is primarily produced in massive stars, following iron production. The combination of the aluminum indices with the FeCr gave the [AlFeCr]. This combined NIR index stands out as the best tracer of the total metal content of galaxies.

Finding an age indicator in the NIR, suitable both for young and old stellar populations has always been challenging. Riffel et al. (2007, 2008, 2009) identified the CN and CO bands as an age proxy for young stellar populations of starbust and active galaxies. Baldwin et al. (2018) analysed the behaviour of some atomic and molecular NIR indices (CN, Mg, Ca, CO, Na, Fe) in normal galaxies and

concluded that age variation in the NIR is subtle. In this paper, we looked for different NIR indices to find a connection with Hβ, hence with age. The resulting T1 index emerges as an excellent NIR tracer of optical Hβ, exhibiting no detectable metallicity scattering within the considered range (−0.7 < [Z/H] < 0.55) of our sample.

We finally tested the best age and metallicity tracers found ([AlFeCr] and T1) with the predictions from the theoretical EMILES and XSL NIR models. The tested SSP models yielded interesting results in the NIR, demonstrating a general agreement with the data. However, they are still not sufficiently accurate or consistent with each other to enable a robust quantitative estimation of stellar population properties in the NIR. This enforces the findings of Baldwin et al. (2018) and Riffel et al. (2019) and extends their conclusions also to the XSL models. Consequently, our new NIR indices sensitive to age and metallicity cannot be currently utilized for directly interpolating the NIR index–index grids produced by the models and estimate the age and metallicities of the stellar populations, until further fine tuning of the models. Nevertheless, these new NIR indices are highly valuable for focusing the model improvements and for retrieving the optical stellar population parameters throughout the estimation of the Lick/IDS counterparts Hβ, Mgb, Mg2, and <Fe> with the provided equations (3), (4), (5), (6), (7), (8), and (10).

Our sample spans a wide range of stellar ages, velocity dispersion, and galaxy morphological types. We did not observe secondary trends due to morphological types and/or velocity dispersion in the correlations between our new NIR indices and the Lick/IDS ones. However, the sample lacks low-metallicity galaxies, and therefore our results are limited to [Z/H] ≳ −0.7 for now. Some rather weak indices are used to build the combined [AlFeCr] and T1 indices, especially for the FeCr (<EW> ≲ 1) and require high S/N spectra ties (S/N ∼ 100 at R ∼ 2000) to obtain reasonably accurate age and metallicity estimates. Moreover, since the targeted features span from the CaT wavelength (λ ∼ 0.85 μm) to the Al1 (λ ∼ 1.7 μm), they require broad-band NIR spectra to be measured. Even at modestly high redshift (≳0.02), some of the indices considered

here will be shifted into wavelength regimes heavily affected by telluric absorption (especially the Al) and alternative indices will have to be considered in future works.

We also built a new composite index $\Sigma 1$ to be more sensitive to velocity dispersion by combining the Al1 index with Mg2h and normalizing by the CaT index, which is known to have a strong anticorrelation with velocity dispersion. The $\Sigma 1$ index results to be a velocity dispersion (hence mass) tracer as good as the optical Mg2 index.

These new age, metallicity, and velocity dispersion indicators in the NIR are suitable in situations, where the optical features might have low S/N (e.g. dust-obscured galaxies) or might not be available due to instrumental constraints, and represent a solid complementary approach to the full spectral fitting method. In the near future, we plan to expand our sample to include low metallicity and higher redshift galaxies to enhance and expand the constraints of the new NIR age, metallicity, and velocity dispersion indicators.

ACKNOWLEDGEMENTS

DATA AVAILABILITY

The reduced spectra and data are available upon request to the authors.

REFERENCES

Arentsen A. et al., 2019, A&A, 627, A138
Baldwin C., McDermid R. M., Kuntschner H., Maraston C., Conroy C., 2018, MNRAS, 473, 4698
Bensby T., Feltzing S., Oey M. S., 2014, A&A, 562, A71
Bruzual G., Charlot S., 2003, MNRAS, 344, 1000
Burstein D., Faber S. M., Gaskell C. M., Krumm N., 1984, ApJ, 287, 586
Cappellari M., Emsellem E., 2004, PASP, 116, 138
Cappellari M. et al., 2011, MNRAS, 413, 813
Cenarro A. J., Cardiel N., Gorgas J., Peletier R. F., Vazdekis A., Prada F., 2001, MNRAS, 326, 959
Cenarro A. J., Gorgas J., Vazdekis A., Cardiel N., Peletier R. F., 2003, MNRAS, 339, L12
Cesetti M. et al., 2009, A&A, 497, 41
Cesetti M., Pizzella A., Ivanov V. D., Morelli L., Corsini E. M., Dalla Bontà E., 2013, A&A, 549, A129
Conroy C., van Dokkum P., 2012, ApJ, 747, 69
Conroy C., Villaume A., van Dokkum P. G., Lind K., 2018, ApJ, 854, 139
Corsini E. M. et al., 2018, A&A, 618, A172
Costantin L., Corsini E. M., Méndez-Abreu J., Morelli L., Dalla Bontà E., Pizzella A., 2018, MNRAS, 481, 3623
Costantin L. et al., 2019, A&A, 632, A9
Cushing M. C., Rayner J. T., Vacca W. D., 2005, ApJ, 623, 1115
Ditrani F. R. et al., 2023, A&A, 677, A93
Eftekhari E., Vazdekis A., La Barbera F., 2021, MNRAS, 504, 2190
Eftekhari E., La Barbera F., Vazdekis A., Allende Prieto C., Knowles A. T., 2022, MNRAS, 512, 378
Faber S. M., Friel E. D., Burstein D., Gaskell C. M., 1985, ApJS, 57, 711
Falcón-Barroso J., Peletier R. F., Vazdekis A., Balcells M., 2003, ApJL, 588, L17
François P., Morelli L., Pizzella A., Ivanov V. D., Coccato L., Cesetti M., Corsini E. M., Dalla Bontà E., 2019, A&A, 621, A60
Freudling W., Romaniello M., Bramich D. M., Ballester P., Forchi V., García-Dabló C. E., Moehler S., Neeser M. J., 2013, A&A, 559, A96
Garcia-Rissmann A., Vega L. R., Asari N. V., Cid Fernandes R., Schmitt H., González Delgado R. M., Storchi-Bergmann T., 2005, MNRAS, 359, 765
Gasparri D. et al., 2021, MNRAS, 507, 4669
Goldoni P., Royer F., François P., Horrobin M., Blanc G., Vernet J., Modigliani A., Larsen J., 2006, in McLean I. S., Iye M., eds, Proc. SPIE Conf. Ser. Vol. 6269, Ground-Based and Airborne Instrumentation for Astronomy. SPIE, Bellingham, p. 62692K
Gonneau A. et al., 2020, A&A, 634, A133
Gorgas J., Efstathiou G., Aragon Salamanca A., 1990, MNRAS, 245, 217
Guinouard I., Horville D., Puech M., Hammer F., Amans J.-P., Chemla F., Dekker H., Mazzoleni R., 2006, in Atad-Ettedgui E., Antebi J., Lemke D., eds, Proc. SPIE Conf. Ser. Vol. 6273, Optomechanical Technologies for Astronomy. SPIE, Bellingham, p. 62733R
Ivanov V. D., Rieke M. J., Engelbracht C. W., Alonso-Herrero A., Rieke G. H., Luhman K. L., 2004, ApJS, 151, 387
Johansson J., Thomas D., Maraston C., 2010, MNRAS, 406, 165
Jorgensen I., 1997, MNRAS, 288, 161
Knowles A. T., Sansom A. E., Allende Prieto C., Vazdekis A., 2021, MNRAS, 504, 2286
Kotilainen J. K., Hyvönen T., Reunanen J., Ivanov V. D., 2012, MNRAS, 425, 1057
Kroupa P., 2001, MNRAS, 322, 231
La Barbera F., Ferreras I., Vazdekis A., de la Rosa I. G., de Carvalho R. R., Trevisan M., Falcón-Barroso J., Ricciardelli E., 2013, MNRAS, 433, 3017
Lagattuta D. J., Mould J. R., Forbes D. A., Monson A. J., Pastorello N., Persson S. E., 2017, ApJ, 846, 166
Landsman W. B., 1995, in Shaw R. A., Payne H. E., Hayes J. J. E., eds, ASP Conf. Ser. Vol. 77, Astronomical Data Analysis Software and Systems IV. Astron. Soc. Pac., San Francisco, p. 437
Makarov D., Prugniel P., Terekhova N., Courtois H., Vauglin I., 2014, A&A, 570, A13
Maraston C., 2005, MNRAS, 362, 799
Maraston C., Strömbäck G., 2011, MNRAS, 418, 2785
Maraston C. et al., 2020, MNRAS, 496, 2962
Mármol-Queraltó E. et al., 2009, ApJL, 705, L199
Martín-Navarro I., Vazdekis A., Falcón-Barroso J., La Barbera F., Yıldırım A., van de Ven G., 2018, MNRAS, 475, 3700
Mason R. E. et al., 2015, ApJS, 217, 13
McLean I. S., McGovern M. R., Burgasser A. J., Kirkpatrick J. D., Prato L., Kim S. S., 2003, ApJ, 596, 561
Meneses-Goytia S., Peletier R. F., Trager S. C., Vazdekis A., 2015, A&A, 582, A97
Morelli L. et al., 2004, MNRAS, 354, 753
Morelli L. et al., 2008, MNRAS, 389, 341
Morelli L., Pizzella A., Corsini E. M., Dalla Bontà E., Coccato L., Méndez-Abreu J., Parmiggiani M., 2015, Astron. Nachr., 336, 208
Morelli L., Parmiggiani M., Corsini E. M., Costantin L., Dalla Bontà E., Méndez-Abreu J., Pizzella A., 2016, MNRAS, 463, 4396
Morelli L. et al., 2020, A&A, 641, 55
Mouhcine M., Lançon A., 2002, A&A, 393, 149
Oliva E., Origlia L., Kotilainen J. K., Moorwood A. F. M., 1995, A&A, 301, 55

Origlia L., Moorwood A. F. M., Oliva E., 1993, A&A, 280, 536

Origlia L., Ferraro F. R., Fusi Pecci F., Oliva E., 1997, A&A, 321, 859

Pietrinferni A., Cassisi S., Salaris M., 2004, Mem. Soc. Astron. Italiana, 75, 170

Pignatari M. et al., 2016, ApJS, 225, 24

Rampazzo R., Panuzzo P., Vega O., Marino A., Bressan A., Clemens M. S., 2013, MNRAS, 432, 374

Rayner J. T., Cushing M. C., Vacca W. D., 2009, ApJS, 185, 289

Rieke G. H., Lebofsky M. J., Thompson R. I., Low F. J., Tokunaga A. T., 1980, ApJ, 238, 24

Riffel R., Pastoriza M. G., Rodríguez-Ardila A., Maraston C., 2007, ApJ, 659, L103

Riffel R., Pastoriza M. G., Rodríguez-Ardila A., Maraston C., 2008, MNRAS, 388, 803

Riffel R., Pastoriza M. G., Rodríguez-Ardila A., Bonatto C., 2009, MNRAS, 400, 273

Riffel R., Ruschel-Dutra D., Pastoriza M. G., Rodríguez-Ardila A., Santos J. F. C. J., Bonatto C. J., Ducati J. R., 2011, MNRAS, 410, 2714

Riffel R. A. et al., 2015, MNRAS, 446, 2823

Riffel R. et al., 2019, MNRAS, 486, 3228

Röck B., Vazdekis A., Peletier R. F., Knapen J. H., Falcón-Barroso J., 2015, MNRAS, 449, 2853

Röck B., Vazdekis A., Ricciardelli E., Peletier R. F., Knapen J. H., Falcón-Barroso J., 2016, A&A, 589, A73

Röck B., Vazdekis A., La Barbera F., Peletier R. F., Knapen J. H., Allende-Prieto C., Aguado D. S., 2017, MNRAS, 472, 361

Sánchez-Blázquez P., Gorgas J., Cardiel N., González J. J., 2006, A&A, 457, 809

Sarzi M. et al., 2006, MNRAS, 366, 1151

Schiavon R. P., 2007, ApJS, 171, 146

Silva D. R., Boroson T. A., Elston R., Rich R. M., 1994, in McLean S., ed., Infrared Astronomy with Arrays, The Next Generation. Springer, The Netherlands, 525

Silva D. R., Kuntschner H., Lyubenova M., 2008, ApJ, 674, 194

Smette A. et al., 2015, A&A, 576, A77

Thomas D., Maraston C., Bender R., 2003, MNRAS, 339, 897

Trager S. C., Worthey G., Faber S. M., Burstein D., González J. J., 1998, ApJS, 116, 1

Trager S. C., Faber S. M., Worthey G., González J. J., 2000, AJ, 120, 165

Vazdekis A., Sánchez-Blázquez P., Falcón-Barroso J., Cenarro A. J., Beasley M. A., Cardiel N., Gorgas J., Peletier R. F., 2010, MNRAS, 404, 1639

Vazdekis A. et al., 2015, MNRAS, 449, 1177

Vazdekis A., Koleva M., Ricciardelli E., Röck B., Falcón-Barroso J., 2016, MNRAS, 463, 3409

Verro K. et al., 2022a, A&A, 660, A34

Verro K. et al., 2022b, A&A, 661, A50

Villaume A., Conroy C., Johnson B., Rayner J., Mann A. W., van Dokkum P., 2017, ApJS, 230, 23

Worthey G., Ottaviani D. L., 1997, ApJS, 111, 377

Worthey G., Faber S. M., Gonzalez J. J., Burstein D., 1994, ApJS, 94, 687

APPENDIX A: NIR SPECTRA OF THE SAMPLE GALAXIES

The NIR portion of the spectra of the sample galaxies and the central wavelength of the NIR indices used as age, metallicity, and velocity dispersion indicators are showed in Figs A1–A7.

Figure A1. NIR spectra of the sample galaxies. The vertical red lines mark the central wavelength of the NIR indices used to define age, metallicity, and velocity dispersion indicators in this paper.

Figure A2. Continued.

Figure A3. Continued.

Figure A4. Continued.

Figure A5. Continued.

Figure A6. Continued.

Figure A7. Continued.

APPENDIX B: NIR INDICES AND EQUIVALENT WIDTHS OF THE NIR LINE-STRENGTH INDICES OF THE SAMPLE

The NIR line-strength index definition and the EWs for all the sample galaxies are given in Tables B1, B2, B3, and B4, respectively.

Table B1. The 39 NIR line-strength indices investigated in this paper.

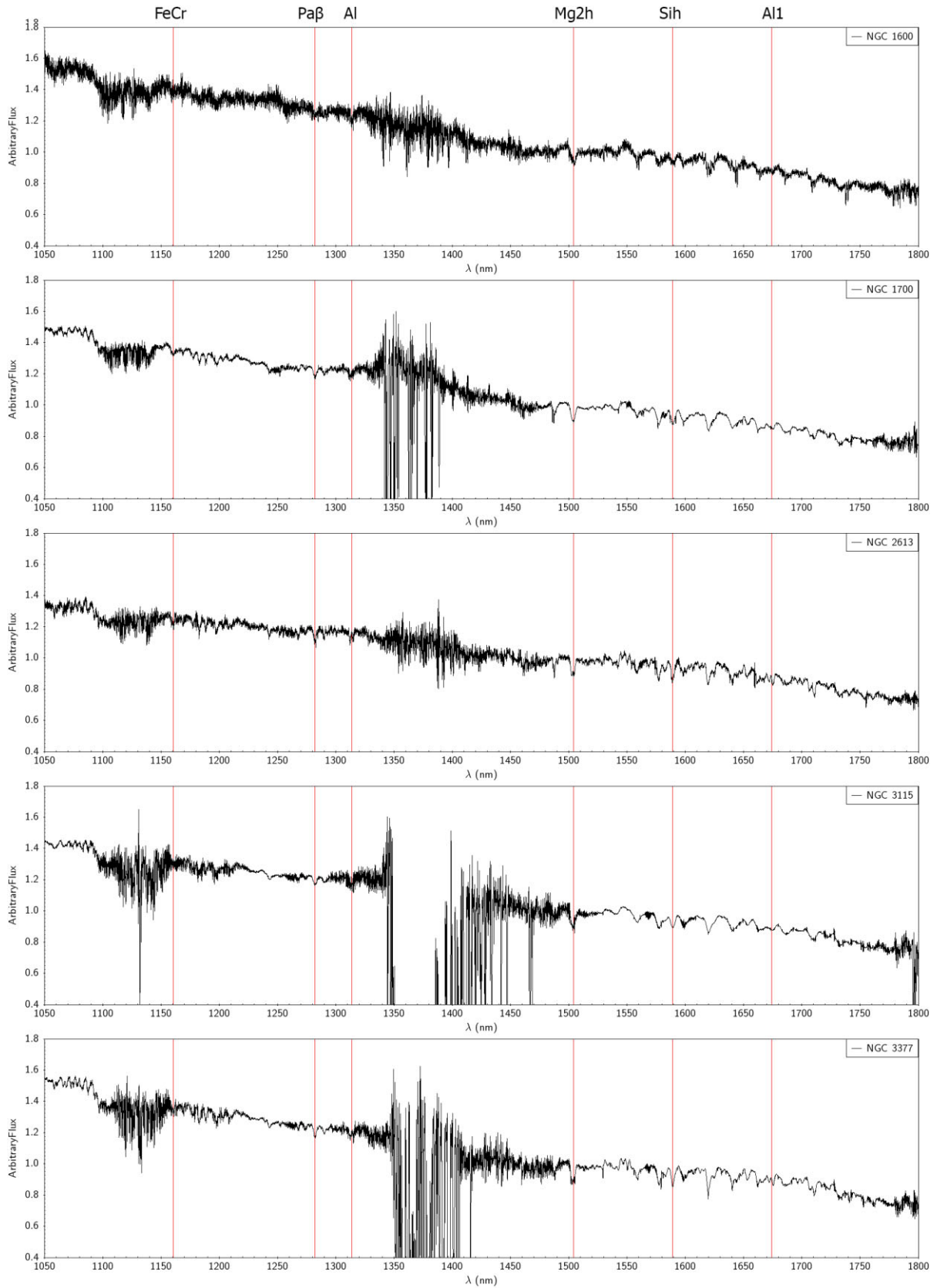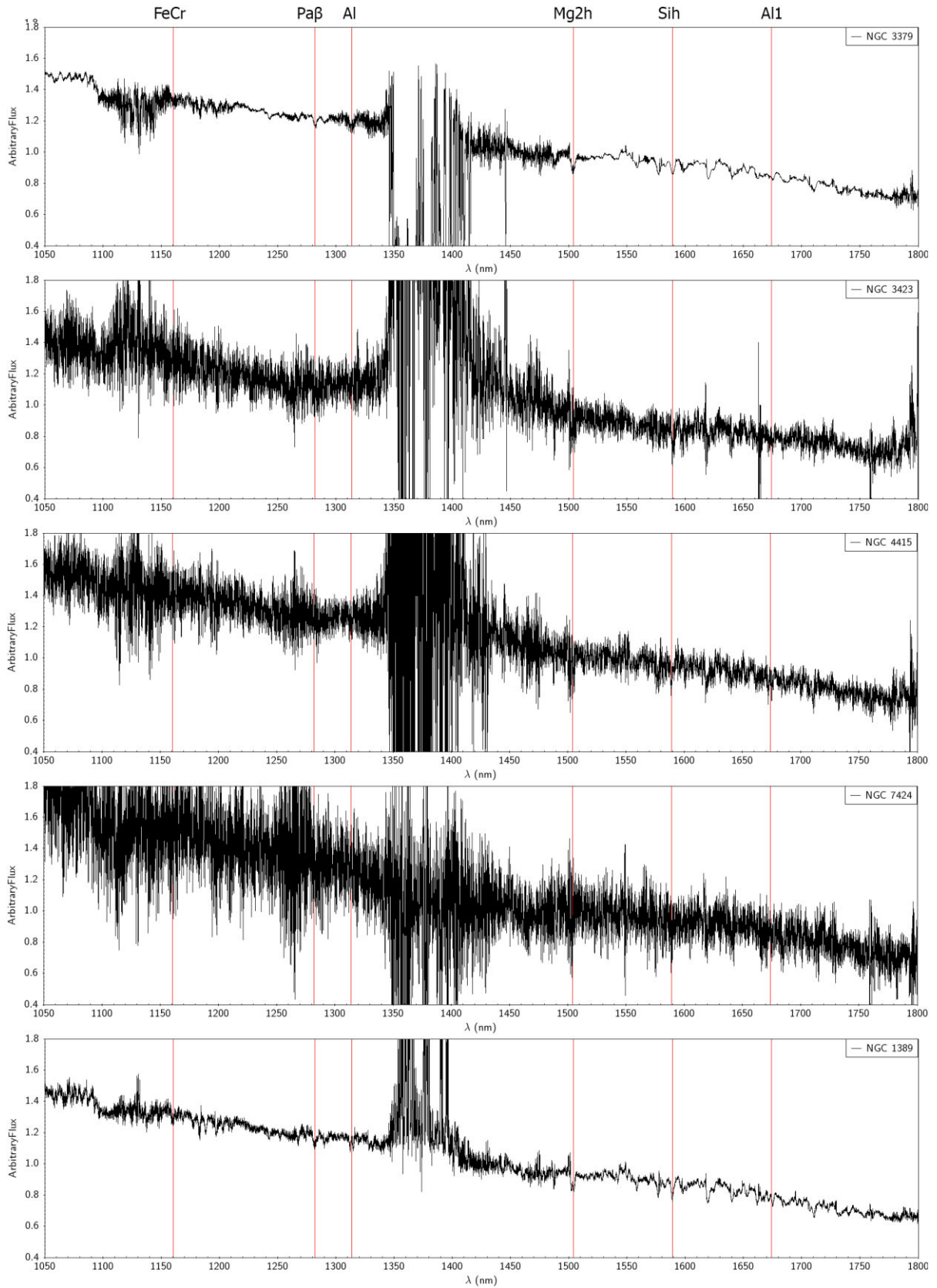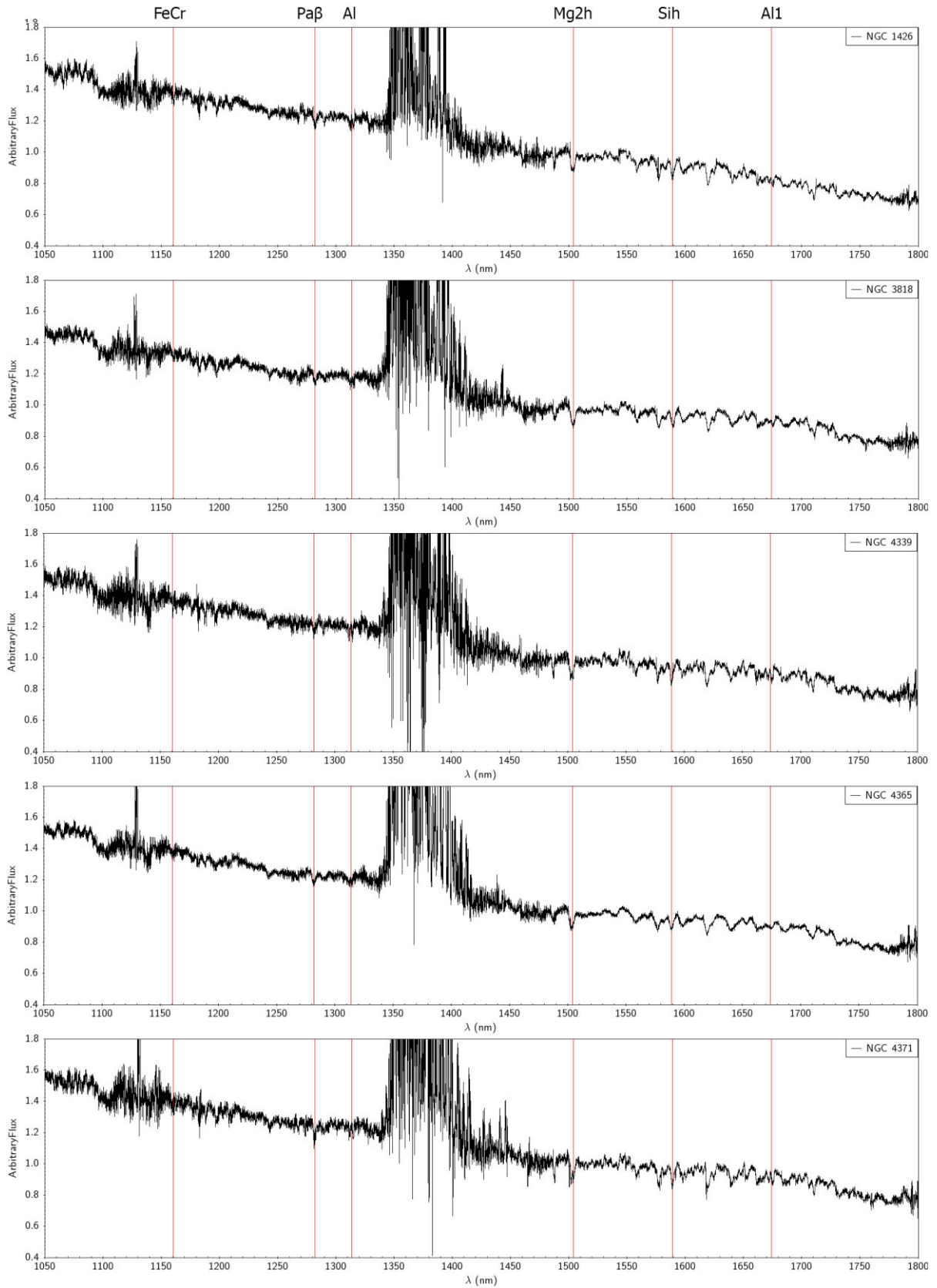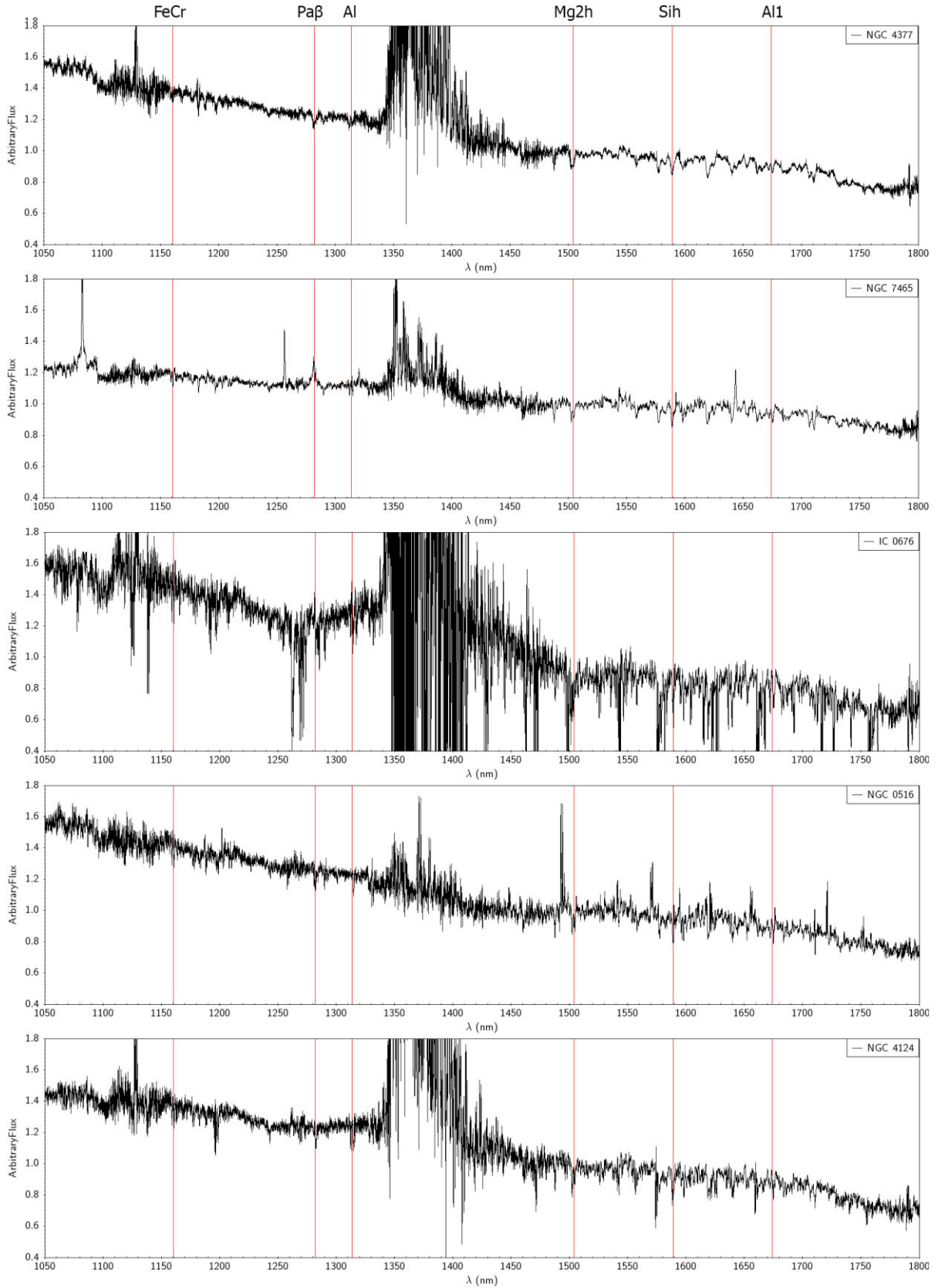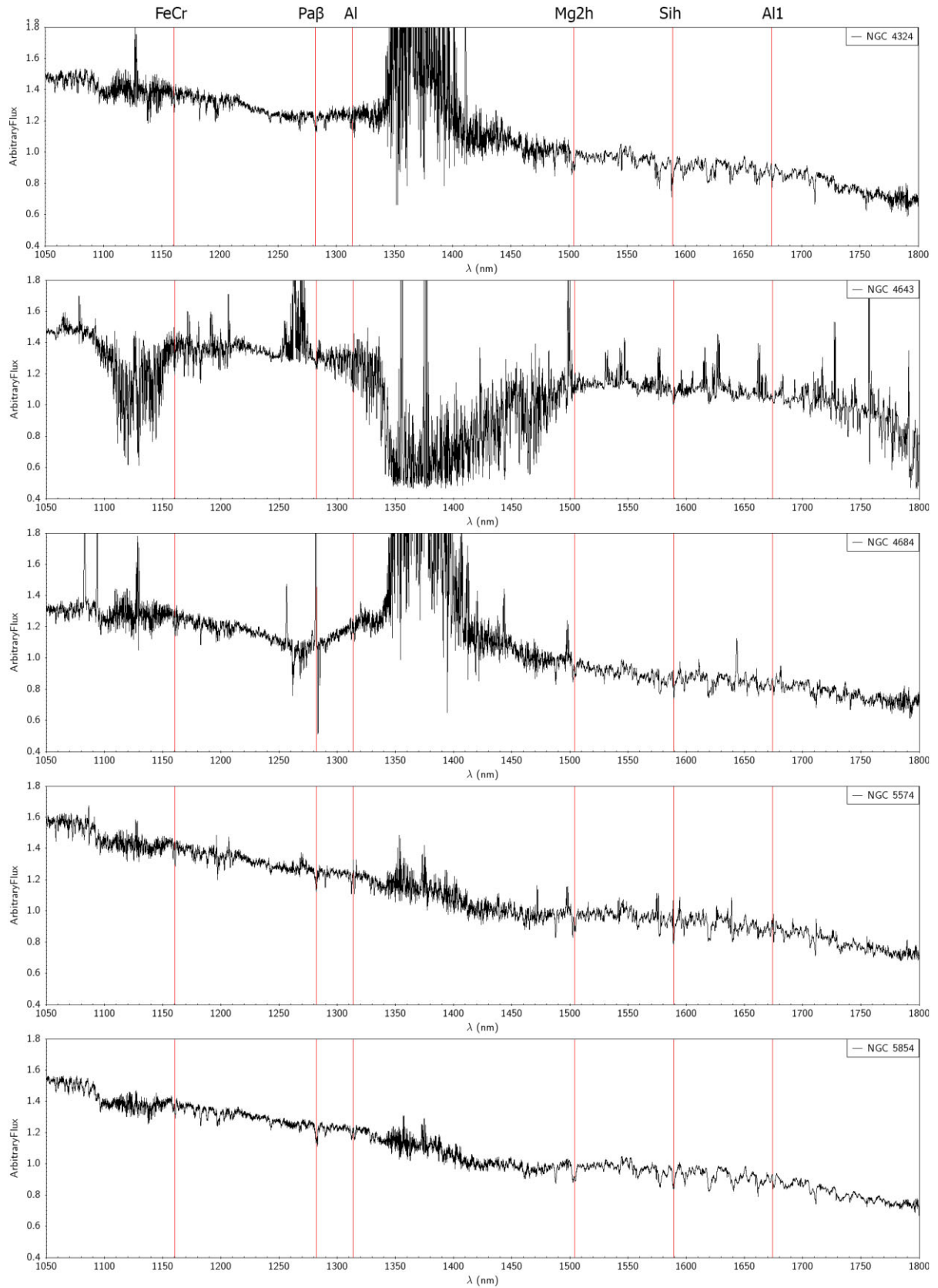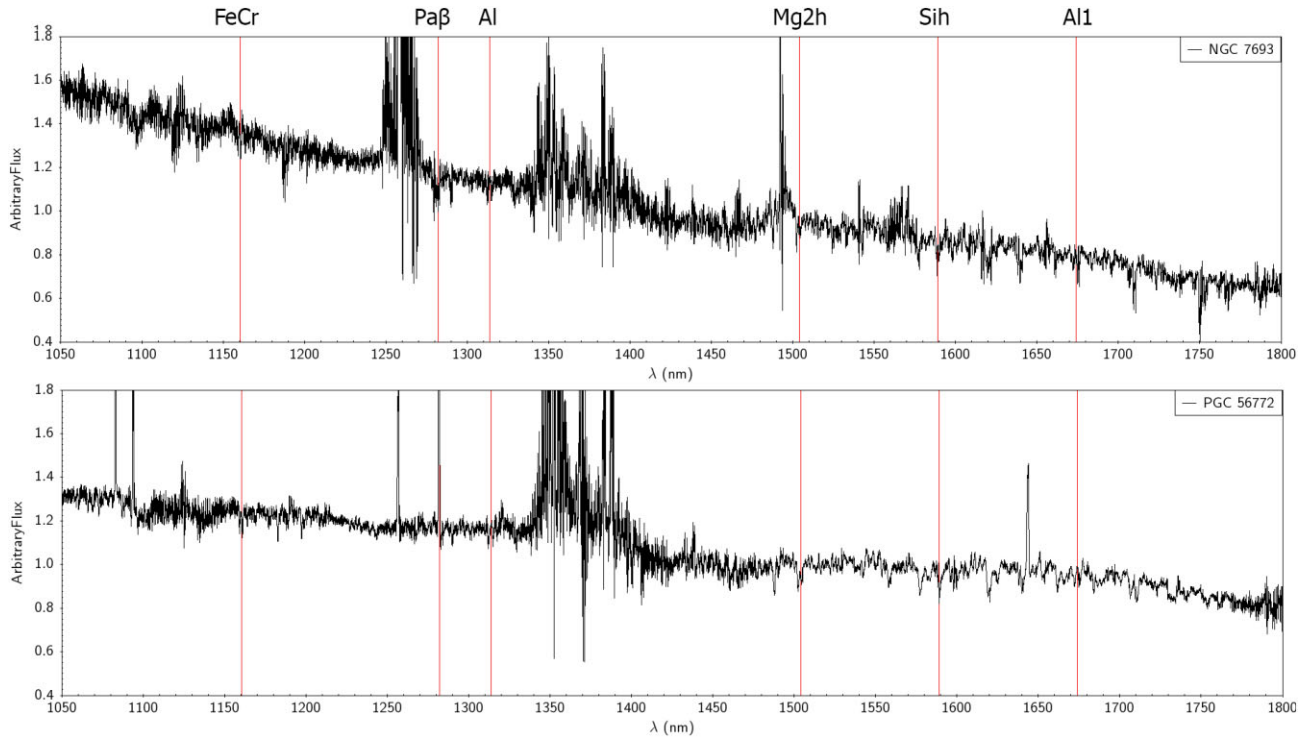| Index name	Dominated by	Line limits (μm)	Blue continuum (μm)	Red continuum (μm)	Main reference	Additional reference
Ca1	Ca II	0.8484–0.8513	0.8474–0.8484	0.8563–0.8577	2	–
Ca2	Ca II	0.8522–0.8562	0.8474–0.8484	0.8563–0.8577	2	–
Ca3	Ca II	0.8642–0.8682	0.8619–0.8642	0.8700–0.8725	2	–
Mgi	Mg I	0.8802–0.8811	0.8776–0.8792	0.8815–0.8850	3	–
Pa5	H I	0.900–0.903	0.8983–0.8998	0.9040–0.9030	3	–
Ti	Ti I	0.9780–0.9795	0.9750–0.9760	0.9800–0.9810	1	–
FeH	FeH	0.9900–0.9950	0.9840–0.9850	0.9985–0.9995	1	9, 10
Paδ	H I	1.0040–1.0067	1.0020–1.0030	1.0067–1.0077	1	–
FeTi	Fe I, Ti I	1.0390–1.0408	1.0198–1.0210	1.0438–1.0446	1	–
Na	Na I	1.1358–1.1428	1.1320–1.1340	1.1430–1.1460	1	–
FeCr	Fe I + Cr I	1.1600–1.1624	1.1560–1.1585	1.1716–1.1746	1	–
K1A	K I	1.1670–1.1714	1.1560–1.1585	1.1716–1.1746	1	9, 10
K1B	K I	1.1765–1.1800	1.1716–1.1746	1.1805–1.1815	1	9, 10
Sij	Si I	1.1977–1.2004	1.1910–1.1935	1.2050–1.2070	1	–
SiMg	Si I, Mg I	1.2070–1.2095	1.2050–1.2070	1.2050–1.2070	1	–
K2A	K I	1.2415–1.2455	1.2350–1.2380	1.2460–1.2490	1	7, 10
Paβ	H I	1.2795–1.2840	1.2755–1.2780	1.2855–1.2873	1	–
Al	Al I	1.3115–1.3168	1.3050–1.3075	1.3230–1.3250	1	9, 11
Mg1h	Mg I	1.4850–1.4910	1.4830–1.4850	1.4910–1.5000	1	7
Mg2h	Mg I	1.5000–1.5080	1.4910–1.5000	1.5100–1.5120	1	7, 4
CO1	$^{12}CO(2,0)$	1.5570–1.5635	1.5480–1.5500	1.5930–1.5940	1	7
Br$_{15}$	H I	1.5670–1.5720	1.5480–1.5500	1.5930–1.5940	1	–
Mg3h	Mg I	1.5730–1.5800	1.5480–1.5500	1.5930–1.5940	1	7
FeH1	FeH	1.5820–1.5860	1.5480–1.5500	1.5930–1.5940	1	4, 7, 8
Sih	Si I	1.5870–1.5910	1.5480–1.5500	1.5930–1.5940	1	4, 7, 8
CO2	$^{12}CO(2,0)$	1.5950–1.6000	1.5930–1.5940	1.6160–1.6180	1	7
CO3	$^{12}CO(2,0)$	1.6180–1.6220	1.6160–1.6180	1.6340–1.6370	1	8
CO4	$^{12}CO(2,0)$	1.6390–1.6470	1.6340–1.6370	1.6585–1.6605	1	–
CO5	$^{12}CO(2,0)$	1.6605–1.6640	1.6585–1.6605	1.6775–1.6790	1	–
Al1	Al I	1.6705–1.6775	1.6585–1.6605	1.6775–1.6790	1	–
COMg	$^{12}CO(2, 0)$, Mg I	1.7050–1.7130	1.6920–1.6960	1.7140–1.7160	1	4
Br$_{10}$	H I	1.7350–1.7390	1.7250–1.7280	1.7440–1.7480	1	–
Mg1k	Mg I	2.1040–2.1110	2.1000–2.1040	2.1110–2.1150	4	–
Nadk	Na I	2.2000–2.2140	2.1934–2.1996	2.2150–2.2190	6	–
FeA	Fe I	2.2250–2.2299	2.2133–2.2176	2.2437–2.2497	5	–
FeB	Fe I	2.2368–2.2414	2.2133–2.2176	2.2437–2.2497	5	–
Ca$_d$	Ca I	2.2594–2.2700	2.2516–2.2590	2.2716–2.2888	6	–
Mg2k	Mg I	2.2795–2.2845	2.2700–2.2720	2.2850–2.2874	5	–
CO12	$^{12}CO(2,0)$	2.2910–2.3070	2.2516–2.2590	2.2716–2.2888	3	–

The references are 1 = Morelli et al. (2020); 2 = Cenarro et al. (2001); 3 = Cesetti et al. (2013); 4 = Ivanov et al. (2004); 5 = Silva et al. (2008); 6 = Cesetti et al. (2009); 7 = Riffel et al. (2019); 8 = Origlia, Moorwood & Oliva (1993); 9 = Conroy & van Dokkum (2012); Villaume et al. (2017); 10 = McLean et al. (2003); Cushing, Rayner & Vacca (2005), 11 = Röck et al. (2015).

Table B2. The equivalent widths in Å of the NIR line-strength indices of the sample galaxies. Part I.

Galaxy	Ca1	Ca2	Ca3	Mgi	Pa5	Ti	FeH	Paδ	FeTi	Na	FeCr	K1A	K1B
NGC 0584	1.342 ± 0.024	3.463 ± 0.025	2.460 ± 0.047	0.360 ± 0.044	1.714 ± 0.021	0.599 ± 0.017	1.238 ± 0.069	0.626 ± 0.044	0.520 ± 0.034	3.018 ± 0.126	0.795 ± 0.029	0.768 ± 0.058	0.759 ± 0.033
NGC 0636	1.388 ± 0.023	3.626 ± 0.022	3.158 ± 0.040	0.696 ± 0.039	1.390 ± 0.035	0.499 ± 0.013	0.669 ± 0.047	0.587 ± 0.037	0.482 ± 0.028	1.881 ± 0.054	0.680 ± 0.028	0.561 ± 0.049	−0.260 ± 0.064
NGC 0897	1.434 ± 0.036	3.643 ± 0.038	2.871 ± 0.041	0.568 ± 0.099	0.870 ± 0.049	0.561 ± 0.028	1.305 ± 0.095	0.615 ± 0.055	0.344 ± 0.031	1.740 ± 0.074	0.643 ± 0.015	0.405 ± 0.031	0.951 ± 0.026
NGC 1357	1.329 ± 0.021	3.588 ± 0.020	3.110 ± 0.039	0.684 ± 0.042	1.420 ± 0.040	0.572 ± 0.023	0.764 ± 0.071	0.518 ± 0.038	0.245 ± 0.021	2.516 ± 0.060	0.747 ± 0.018	0.447 ± 0.033	0.388 ± 0.034
NGC 1425	1.372 ± 0.015	3.672 ± 0.012	3.111 ± 0.039	0.586 ± 0.039	1.160 ± 0.023	0.576 ± 0.042	0.588 ± 0.027	0.735 ± 0.049	0.260 ± 0.026	1.451 ± 0.049	0.709 ± 0.015	0.879 ± 0.036	0.117 ± 0.150
NGC 1600	0.989 ± 0.038	3.234 ± 0.048	3.119 ± 0.074	0.714 ± 0.127	0.590 ± 0.041	0.356 ± 0.054	−0.304 ± 0.061	–	0.329 ± 0.061	1.548 ± 0.091	0.455 ± 0.041	–	–
NGC 1700	1.324 ± 0.031	–	–	1.485 ± 0.138	0.880 ± 0.093	−0.046 ± 0.103	2.225 ± 0.166	–	0.463 ± 0.034	1.918 ± 0.071	0.779 ± 0.030	0.589 ± 0.053	1.190 ± 0.026
NGC 2613	1.348 ± 0.022	3.455 ± 0.021	3.179 ± 0.044	0.683 ± 0.043	1.306 ± 0.012	0.691 ± 0.027	0.852 ± 0.050	0.761 ± 0.036	0.156 ± 0.016	1.934 ± 0.083	0.637 ± 0.016	0.851 ± 0.043	0.910 ± 0.029
NGC 3115	1.229 ± 0.029	3.493 ± 0.037	2.984 ± 0.049	0.635 ± 0.112	–	–	0.280 ± 0.075	0.524 ± 0.037	0.540 ± 0.046	−0.763 ± 0.393	0.458 ± 0.040	0.530 ± 0.067	1.241 ± 0.084
NGC 3377	1.393 ± 0.019	3.599 ± 0.016	3.062 ± 0.037	0.558 ± 0.040	–	0.256 ± 0.029	0.453 ± 0.045	0.659 ± 0.033	0.400 ± 0.020	−0.361 ± 0.233	0.378 ± 0.012	0.283 ± 0.022	1.322 ± 0.029
NGC 3379	1.318 ± 0.027	3.323 ± 0.028	2.867 ± 0.046	0.936 ± 0.061	–	0.794 ± 0.070	0.029 ± 0.057	0.575 ± 0.062	0.441 ± 0.032	1.772 ± 0.339	0.621 ± 0.021	0.716 ± 0.047	0.757 ± 0.033
NGC 3423	1.889 ± 0.109	3.905 ± 0.133	3.017 ± 0.076	0.242 ± 0.081	–	–	–	–	–	2.330 ± 0.512	0.243 ± 0.134	–	0.206 ± 0.195
NGC 4415	1.260 ± 0.068	3.407 ± 0.083	3.026 ± 0.114	0.686 ± 0.061	–	0.363 ± 0.105	0.089 ± 0.139	–	–	4.051 ± 0.450	0.318 ± 0.064	–	0.682 ± 0.047
NGC 7424	1.403 ± 0.043	3.647 ± 0.048	3.892 ± 0.132	0.402 ± 0.056	0.641 ± 0.069	0.267 ± 0.103	–	–	–	0.455 ± 0.395	1.176 ± 0.215	–	1.475 ± 0.283
NGC 7465	1.274 ± 0.037	3.441 ± 0.042	2.812 ± 0.061	0.480 ± 0.039	0.952 ± 0.033	0.435 ± 0.017	1.576 ± 0.113	–	0.471 ± 0.024	0.904 ± 0.126	0.518 ± 0.017	0.624 ± 0.034	0.823 ± 0.026
IC 0676	1.581 ± 0.029	3.564 ± 0.033	3.185 ± 0.132	0.374 ± 0.146	1.749 ± 0.066	0.379 ± 0.109	3.326 ± 0.099	–	0.648 ± 0.055	2.626 ± 0.282	0.300 ± 0.090	0.588 ± 0.134	0.826 ± 0.113
NGC 0516	1.558 ± 0.028	4.059 ± 0.034	3.625 ± 0.093	0.687 ± 0.079	1.042 ± 0.039	0.298 ± 0.022	−0.416 ± 0.063	0.414 ± 0.091	1.235 ± 0.314	0.686 ± 0.126	–	0.549 ± 0.063	0.866 ± 0.042
NGC 4124	1.481 ± 0.036	3.776 ± 0.043	3.335 ± 0.100	0.568 ± 0.055	1.347 ± 0.041	0.563 ± 0.024	1.558 ± 0.139	0.301 ± 0.073	0.784 ± 0.034	3.446 ± 0.196	0.810 ± 0.071	0.523 ± 0.106	0.925 ± 0.086
NGC 4324	1.430 ± 0.027	3.779 ± 0.030	3.349 ± 0.059	0.668 ± 0.051	1.063 ± 0.035	0.693 ± 0.030	1.360 ± 0.041	–	0.677 ± 0.029	1.844 ± 0.120	0.656 ± 0.038	0.523 ± 0.059	0.857 ± 0.031
NGC 4643	1.214 ± 0.026	3.409 ± 0.030	3.781 ± 0.091	0.797 ± 0.066	0.360 ± 0.071	0.662 ± 0.066	–	0.737 ± 0.074	0.856 ± 0.042	5.171 ± 1.097	0.789 ± 0.186	–	–
NGC 4684	1.029 ± 0.036	3.076 ± 0.044	2.549 ± 0.058	0.643 ± 0.051	0.373 ± 0.060	0.747 ± 0.029	1.158 ± 0.066	–	0.439 ± 0.017	1.224 ± 0.138	0.559 ± 0.042	0.536 ± 0.063	0.859 ± 0.057
NGC 5574	1.468 ± 0.030	4.090 ± 0.036	3.685 ± 0.067	0.602 ± 0.044	1.409 ± 0.030	0.668 ± 0.036	0.679 ± 0.064	0.657 ± 0.038	0.483 ± 0.012	0.711 ± 0.143	0.869 ± 0.018	0.758 ± 0.029	0.973 ± 0.024
NGC 5854	1.433 ± 0.019	3.865 ± 0.019	3.310 ± 0.041	0.607 ± 0.038	1.240 ± 0.016	0.631 ± 0.035	0.334 ± 0.047	0.997 ± 0.039	0.623 ± 0.022	1.135 ± 0.097	0.724 ± 0.018	0.682 ± 0.037	0.929 ± 0.010
NGC 7693	1.203 ± 0.039	3.668 ± 0.044	3.238 ± 0.148	0.500 ± 0.074	1.533 ± 0.035	−0.528 ± 0.069	0.820 ± 0.129	–	0.374 ± 0.127	1.714 ± 0.139	0.986 ± 0.037	1.646 ± 0.057	0.573 ± 0.032
PGC 56772	1.148 ± 0.036	3.486 ± 0.043	3.191 ± 0.042	0.528 ± 0.048	0.869 ± 0.036	0.502 ± 0.029	0.773 ± 0.094	0.210 ± 0.054	0.431 ± 0.022	1.187 ± 0.147	0.885 ± 0.023	0.542 ± 0.036	0.609 ± 0.019
NGC 1389	1.499 ± 0.046	3.656 ± 0.052	3.168 ± 0.091	0.861 ± 0.049	0.816 ± 0.031	0.512 ± 0.106	0.574 ± 0.085	0.312 ± 0.058	0.360 ± 0.054	1.478 ± 0.106	0.762 ± 0.038	0.668 ± 0.059	1.108 ± 0.036
NGC 1426	1.388 ± 0.037	3.852 ± 0.041	3.146 ± 0.065	0.671 ± 0.074	0.942 ± 0.025	0.429 ± 0.055	–	0.622 ± 0.119	0.067 ± 0.019	1.769 ± 0.121	0.685 ± 0.026	0.413 ± 0.044	0.426 ± 0.052
NGC 3818	1.310 ± 0.066	3.390 ± 0.074	2.754 ± 0.059	0.694 ± 0.084	0.976 ± 0.042	0.882 ± 0.060	−0.068 ± 0.185	0.013 ± 0.029	0.174 ± 0.026	0.946 ± 0.080	0.672 ± 0.042	0.748 ± 0.076	0.994 ± 0.058
NGC 4339	1.544 ± 0.043	4.020 ± 0.051	3.464 ± 0.088	0.863 ± 0.065	0.917 ± 0.043	0.843 ± 0.077	0.759 ± 0.114	0.703 ± 0.062	0.180 ± 0.017	2.712 ± 0.138	0.855 ± 0.045	0.772 ± 0.074	1.164 ± 0.038
NGC 4365	1.405 ± 0.045	3.574 ± 0.050	3.076 ± 0.053	1.001 ± 0.093	0.776 ± 0.045	0.741 ± 0.122	1.051 ± 0.152	0.644 ± 0.076	0.108 ± 0.031	2.468 ± 0.112	0.636 ± 0.035	0.702 ± 0.062	0.634 ± 0.075
NGC 4371	1.402 ± 0.032	3.824 ± 0.035	3.336 ± 0.068	0.795 ± 0.041	1.054 ± 0.047	0.260 ± 0.068	0.834 ± 0.156	0.968 ± 0.105	0.120 ± 0.033	1.718 ± 0.256	0.866 ± 0.047	1.053 ± 0.081	1.142 ± 0.051
NGC 4377	1.303 ± 0.030	3.489 ± 0.034	2.792 ± 0.056	0.626 ± 0.043	0.841 ± 0.044	0.574 ± 0.080	0.307 ± 0.145	1.069 ± 0.059	0.049 ± 0.028	1.904 ± 0.124	0.565 ± 0.025	0.651 ± 0.047	0.787 ± 0.037

Table B3. The equivalent widths in Å of the NIR line-strength indices of the sample galaxies. Part II.

Galaxy	Sij	SiMg	K2A	Paβ	Al	Mg1h	Mg2h	CO1	Br15	Mg3h	FeH1	Sih	CO2
NGC 0584	0.858 ± 0.019	0.525 ± 0.024	1.118 ± 0.029	1.756 ± 0.025	1.939 ± 0.033	1.818 ± 0.057	4.566 ± 0.091	4.651 ± 0.078	1.246 ± 0.068	6.467 ± 0.080	2.021 ± 0.071	4.199 ± 0.064	3.344 ± 0.117
NGC 0636	1.043 ± 0.018	0.515 ± 0.035	1.021 ± 0.028	1.829 ± 0.022	1.582 ± 0.035	2.002 ± 0.065	4.687 ± 0.086	4.637 ± 0.072	1.716 ± 0.066	5.938 ± 0.074	1.885 ± 0.061	3.781 ± 0.056	3.311 ± 0.094
NGC 0897	1.042 ± 0.017	0.457 ± 0.021	1.516 ± 0.040	1.377 ± 0.024	1.814 ± 0.030	1.929 ± 0.063	4.657 ± 0.112	4.804 ± 0.052	1.559 ± 0.051	5.518 ± 0.052	1.861 ± 0.053	4.037 ± 0.041	3.055 ± 0.109
NGC 1357	1.011 ± 0.021	0.565 ± 0.026	1.076 ± 0.021	1.503 ± 0.024	1.770 ± 0.032	1.932 ± 0.053	4.686 ± 0.090	4.225 ± 0.109	1.619 ± 0.103	6.174 ± 0.114	2.081 ± 0.084	3.833 ± 0.085	3.459 ± 0.096
NGC 1425	0.830 ± 0.014	0.534 ± 0.014	0.602 ± 0.018	1.609 ± 0.025	1.067 ± 0.028	1.716 ± 0.062	3.994 ± 0.073	3.852 ± 0.123	1.230 ± 0.109	5.651 ± 0.120	2.129 ± 0.095	4.240 ± 0.092	3.237 ± 0.079
NGC 1600	1.119 ± 0.046	0.475 ± 0.040	—	1.262 ± 0.039	1.925 ± 0.045	1.293 ± 0.076	4.495 ± 0.161	5.514 ± 0.061	1.385 ± 0.067	4.954 ± 0.064	1.441 ± 0.064	2.949 ± 0.062	3.101 ± 0.218
NGC 1700	0.860 ± 0.016	0.399 ± 0.027	0.739 ± 0.030	1.637 ± 0.026	2.027 ± 0.050	2.358 ± 0.075	4.751 ± 0.107	4.245 ± 0.050	1.425 ± 0.048	5.636 ± 0.050	1.569 ± 0.048	3.850 ± 0.038	3.276 ± 0.126
NGC 2613	0.796 ± 0.015	0.633 ± 0.016	0.844 ± 0.025	1.849 ± 0.025	1.544 ± 0.025	1.480 ± 0.047	4.460 ± 0.069	4.049 ± 0.131	1.275 ± 0.113	5.277 ± 0.127	1.555 ± 0.108	4.083 ± 0.102	3.019 ± 0.125
NGC 3115	0.620 ± 0.023	0.289 ± 0.042	1.144 ± 0.034	1.508 ± 0.029	2.074 ± 0.044	2.413 ± 0.082	4.936 ± 0.121	4.703 ± 0.043	1.010 ± 0.038	5.768 ± 0.046	1.784 ± 0.055	3.958 ± 0.037	3.143 ± 0.140
NGC 3377	1.009 ± 0.018	0.428 ± 0.026	0.952 ± 0.023	1.553 ± 0.018	1.534 ± 0.052	2.002 ± 0.053	4.678 ± 0.098	4.582 ± 0.110	0.836 ± 0.099	5.329 ± 0.112	1.736 ± 0.089	3.737 ± 0.089	2.605 ± 0.086
NGC 3379	0.825 ± 0.024	0.382 ± 0.026	1.026 ± 0.031	1.403 ± 0.024	2.021 ± 0.031	2.177 ± 0.075	4.040 ± 0.117	4.713 ± 0.046	1.659 ± 0.046	5.684 ± 0.047	1.904 ± 0.049	3.890 ± 0.036	2.851 ± 0.076
NGC 3423	—	—	—	1.870 ± 0.180	1.689 ± 0.128	2.455 ± 0.322	—	4.731 ± 0.220	1.684 ± 0.199	—	1.551 ± 0.177	3.814 ± 0.177	3.297 ± 0.203
NGC 4415	—	—	—	—	0.903 ± 0.113	—	—	4.053 ± 0.315	1.910 ± 0.261	—	1.806 ± 0.264	3.830 ± 0.252	—
NGC 7424	0.996 ± 0.147	0.865 ± 0.154	1.186 ± 0.259	2.639 ± 0.277	−0.198 ± 0.114	—	—	—	—	—	0.546 ± 0.453	3.372 ± 0.457	—
NGC 7465	0.979 ± 0.029	0.473 ± 0.026	0.727 ± 0.031	2.019 ± 0.043	0.890 ± 0.048	1.449 ± 0.073	3.339 ± 0.104	4.309 ± 0.138	1.472 ± 0.119	4.275 ± 0.147	1.834 ± 0.114	3.394 ± 0.108	2.578 ± 0.077
IC 0676	—	0.102 ± 0.278	0.976 ± 0.106	—	0.976 ± 0.156	—	—	3.000 ± 0.288	0.593 ± 0.257	—	—	4.181 ± 0.232	4.483 ± 0.271
NGC 0516	—	0.057 ± 0.093	1.036 ± 0.059	1.617 ± 0.046	1.156 ± 0.092	—	—	—	—	5.131 ± 0.747	—	—	—
NGC 4124	—	—	1.061 ± 0.124	2.543 ± 0.051	1.434 ± 0.142	—	—	—	—	—	—	—	—
NGC 4324	0.797 ± 0.056	0.183 ± 0.056	0.931 ± 0.026	1.762 ± 0.046	1.938 ± 0.071	1.635 ± 0.120	4.113 ± 0.147	3.783 ± 0.130	1.109 ± 0.119	5.984 ± 0.138	1.413 ± 0.107	3.589 ± 0.104	2.864 ± 0.109
NGC 4643	0.659 ± 0.111	—	0.433 ± 0.039	1.833 ± 0.117	1.582 ± 0.385	2.302 ± 0.548	—	5.319 ± 0.075	1.690 ± 0.065	—	1.264 ± 0.058	3.955 ± 0.055	2.326 ± 0.260
NGC 4684	0.671 ± 0.057	0.390 ± 0.051	0.788 ± 0.052	1.732 ± 0.099	1.048 ± 0.054	2.272 ± 0.213	3.271 ± 0.308	3.906 ± 0.113	2.144 ± 0.098	4.816 ± 0.111	2.439 ± 0.087	3.112 ± 0.084	2.620 ± 0.070
NGC 5574	1.129 ± 0.052	0.552 ± 0.052	0.800 ± 0.024	1.974 ± 0.020	1.210 ± 0.020	2.063 ± 0.192	3.865 ± 0.260	4.236 ± 0.145	1.848 ± 0.129	3.641 ± 0.151	2.273 ± 0.113	3.480 ± 0.116	3.165 ± 0.091
NGC 5854	0.976 ± 0.023	0.413 ± 0.026	0.854 ± 0.023	2.247 ± 0.021	1.513 ± 0.040	1.743 ± 0.062	3.939 ± 0.092	4.557 ± 0.111	1.883 ± 0.092	5.795 ± 0.108	2.023 ± 0.081	3.861 ± 0.082	2.650 ± 0.081
NGC 7693	—	1.001 ± 0.063	−0.447 ± 0.164	3.586 ± 0.159	1.639 ± 0.049	0.517 ± 0.951	—	2.497 ± 0.144	—	7.391 ± 0.151	0.540 ± 0.115	3.718 ± 0.117	3.020 ± 0.394
PGC 56772	0.696 ± 0.062	0.304 ± 0.020	0.709 ± 0.022	1.904 ± 0.046	0.973 ± 0.053	1.556 ± 0.110	3.682 ± 0.099	3.729 ± 0.159	0.752 ± 0.141	4.343 ± 0.163	1.594 ± 0.120	2.789 ± 0.126	2.195 ± 0.070
NGC 1389	0.843 ± 0.026	0.338 ± 0.019	1.045 ± 0.021	2.101 ± 0.037	1.533 ± 0.044	1.447 ± 0.092	3.254 ± 0.151	4.646 ± 0.163	2.035 ± 0.148	5.043 ± 0.172	1.914 ± 0.132	4.249 ± 0.131	3.290 ± 0.074
NGC 1426	1.084 ± 0.017	0.659 ± 0.027	1.029 ± 0.033	1.806 ± 0.029	2.092 ± 0.033	1.750 ± 0.067	4.339 ± 0.147	4.873 ± 0.100	1.720 ± 0.092	5.430 ± 0.109	1.999 ± 0.086	3.707 ± 0.079	3.378 ± 0.092
NGC 3818	1.048 ± 0.027	0.518 ± 0.025	0.960 ± 0.032	1.571 ± 0.034	2.253 ± 0.042	2.305 ± 0.092	5.053 ± 0.165	5.003 ± 0.087	1.832 ± 0.087	5.755 ± 0.090	2.087 ± 0.079	3.854 ± 0.073	3.183 ± 0.120
NGC 4339	0.825 ± 0.030	0.395 ± 0.042	1.029 ± 0.050	1.377 ± 0.053	2.059 ± 0.055	2.125 ± 0.125	4.525 ± 0.125	4.386 ± 0.156	1.747 ± 0.141	5.283 ± 0.161	2.070 ± 0.118	4.017 ± 0.118	2.938 ± 0.082
NGC 4365	0.756 ± 0.028	0.664 ± 0.045	1.264 ± 0.040	1.914 ± 0.047	1.765 ± 0.076	2.148 ± 0.081	4.961 ± 0.158	4.560 ± 0.056	2.025 ± 0.067	6.415 ± 0.061	2.137 ± 0.073	4.602 ± 0.055	3.962 ± 0.217
NGC 4371	1.008 ± 0.035	0.683 ± 0.031	1.243 ± 0.047	1.649 ± 0.044	1.501 ± 0.071	1.946 ± 0.082	4.535 ± 0.107	3.988 ± 0.121	1.403 ± 0.112	5.912 ± 0.128	1.909 ± 0.100	3.974 ± 0.096	3.393 ± 0.223
NGC 4377	0.785 ± 0.016	0.394 ± 0.018	0.857 ± 0.027	1.768 ± 0.024	1.556 ± 0.043	1.443 ± 0.060	3.974 ± 0.109	3.701 ± 0.082	1.404 ± 0.074	4.964 ± 0.082	1.963 ± 0.068	3.956 ± 0.063	3.190 ± 0.108

Table B4. The equivalent widths in Å of the NIR line-strength indices of the sample galaxies. Part III.

Galaxy	CO3	CO4	CO5	AlI	COMg	Br10	MgIk	Nadk	FeA	FeB	Cad	Mg2k	CO12
NGC 0584	5.292 ± 0.115	4.187 ± 0.109	2.279 ± 0.088	3.621 ± 0.197	4.900 ± 0.074	1.239 ± 0.043	1.909 ± 0.102	5.693 ± 0.165	0.980 ± 0.022	1.007 ± 0.040	2.261 ± 0.127	1.209 ± 0.040	23.337 ± 0.159
NGC 0636	4.849 ± 0.086	4.712 ± 0.068	2.512 ± 0.041	3.506 ± 0.125	4.839 ± 0.059	1.163 ± 0.032	1.573 ± 0.066	6.040 ± 0.151	1.513 ± 0.057	0.920 ± 0.061	1.921 ± 0.169	1.110 ± 0.046	21.240 ± 0.211
NGC 0897	5.126 ± 0.117	4.705 ± 0.095	2.693 ± 0.059	3.909 ± 0.206	4.376 ± 0.042	1.685 ± 0.041	1.587 ± 0.097	4.731 ± 0.153	1.048 ± 0.043	−0.004 ± 0.041	2.735 ± 0.081	0.686 ± 0.031	18.550 ± 0.096
NGC 1357	5.115 ± 0.103	4.207 ± 0.092	2.698 ± 0.033	3.393 ± 0.088	4.976 ± 0.083	1.260 ± 0.031	1.719 ± 0.090	5.717 ± 0.108	1.194 ± 0.067	0.696 ± 0.066	–	1.086 ± 0.041	24.540 ± 0.214
NGC 1425	4.534 ± 0.070	4.201 ± 0.166	2.168 ± 0.149	3.186 ± 0.203	4.953 ± 0.079	1.167 ± 0.038	1.059 ± 0.028	3.589 ± 0.119	1.243 ± 0.029	0.688 ± 0.029	3.795 ± 0.108	0.641 ± 0.063	20.204 ± 0.131
NGC 1600	5.373 ± 0.194	4.586 ± 0.099	2.466 ± 0.059	3.860 ± 0.282	4.109 ± 0.059	2.131 ± 0.074	0.648 ± 0.111	3.874 ± 0.341	–	–	–	1.907	–
NGC 1700	4.638 ± 0.126	4.649 ± 0.086	2.765 ± 0.064	3.076 ± 0.176	4.304 ± 0.062	1.396 ± 0.033	1.430 ± 0.083	5.751 ± 0.175	2.106 ± 0.027	1.131 ± 0.044	3.142 ± 0.068	0.326 ± 0.053	20.710 ± 0.089
NGC 2613	4.416 ± 0.098	3.625 ± 0.065	2.178 ± 0.054	3.160 ± 0.113	4.766 ± 0.072	1.070 ± 0.041	1.861 ± 0.063	4.270 ± 0.104	1.041 ± 0.039	0.550 ± 0.039	1.400 ± 0.167	1.390 ± 0.094	23.049 ± 0.215
NGC 3115	4.650 ± 0.146	4.852 ± 0.108	2.495 ± 0.087	3.812 ± 0.268	4.606 ± 0.049	1.225 ± 0.039	1.156 ± 0.089	6.388 ± 0.221	1.226 ± 0.016	0.237 ± 0.016	3.833 ± 0.098	0.623 ± 0.025	23.233 ± 0.113
NGC 3377	4.755 ± 0.077	4.928 ± 0.072	2.745 ± 0.049	3.745 ± 0.119	4.772 ± 0.060	1.177 ± 0.044	1.306 ± 0.058	5.355 ± 0.142	1.499 ± 0.031	0.353 ± 0.028	3.485 ± 0.090	0.820 ± 0.026	23.016 ± 0.110
NGC 3379	4.428 ± 0.081	4.480 ± 0.128	2.394 ± 0.124	3.687 ± 0.240	4.646 ± 0.047	1.065 ± 0.038	1.134 ± 0.068	4.560 ± 0.139	1.101 ± 0.034	0.221 ± 0.031	3.126 ± 0.109	0.664 ± 0.035	22.024 ± 0.140
NGC 3423	4.136 ± 0.149	2.186 ± 0.115	–	2.218 ± 0.091	3.843 ± 0.148	1.403 ± 0.158	–	–	–	–	–	–	–
NGC 4415	3.872 ± 0.164	2.973 ± 0.173	2.660 ± 0.091	3.966 ± 0.131	–	1.065 ± 0.141	–	–	–	–	–	–	–
NGC 7424	5.596 ± 0.272	2.924 ± 0.220	−±0.139	2.618 ± 0.197	–	0.018 ± 0.150	–	–	–	–	–	–	–
IC 0676	4.048 ± 0.067	–	2.610 ± 0.069	3.395 ± 0.098	3.771 ± 0.062	0.462 ± 0.046	0.879 ± 0.055	3.239 ± 0.060	1.558 ± 0.094	1.278 ± 0.091	2.817 ± 0.148	0.994 ± 0.058	7.715 ± 0.196
NGC 0516	3.019 ± 1.674	–	4.639 ± 0.458	2.783 ± 0.431	–	–	–	4.595 ± 2.615	1.527 ± 0.242	0.806 ± 0.101	2.943 ± 0.702	–	13.096 ± 0.462
NGC 4124	4.380 ± 0.627	2.325 ± 0.159	1.770 ± 0.124	2.089 ± 0.164	–	1.198 ± 0.193	1.261 ± 0.291	1.694 ± 0.889	0.650 ± 0.115	1.523 ± 0.110	4.862 ± 0.372	1.551 ± 0.104	49.014 ± 0.562
NGC 4324	4.541 ± 0.090	3.402 ± 0.119	2.291 ± 0.078	2.521 ± 0.094	3.859 ± 0.102	1.057 ± 0.065	1.506 ± 0.059	5.576 ± 0.125	0.953 ± 0.075	1.539 ± 0.070	–	0.978 ± 0.156	–
NGC 4643	–	−±0.150	–	2.417 ± 0.112	4.088 ± 0.263	–	–	–	–	–	–	–	–
NGC 4684	4.382 ± 0.118	5.350 ± 0.133	1.812 ± 0.047	1.528 ± 0.064	3.855 ± 0.141	–	0.647 ± 0.359	3.091 ± 0.170	–	1.197 ± 0.181	–	1.348 ± 0.070	18.364 ± 0.635
NGC 5574	4.496 ± 0.123	4.607 ± 0.084	2.236 ± 0.057	2.402 ± 0.084	4.825 ± 0.129	1.325 ± 0.094	2.168 ± 0.159	4.893 ± 0.105	0.742 ± 0.060	0.496 ± 0.060	–	0.858 ± 0.087	35.969 ± 0.394
NGC 5854	4.698 ± 0.085	–	–	–	4.487 ± 0.068	1.178 ± 0.052	2.193 ± 0.072	5.402 ± 0.115	0.703 ± 0.079	1.054 ± 0.077	–	0.903 ± 0.065	36.301 ± 0.374
NGC 7693	–	4.502 ± 0.095	1.652 ± 0.593	–	–	−1.494 ± 1.230	–	–	–	–	–	0.027 ± 0.108	13.657 ± 1.141
PGC 56772	4.352 ± 0.063	4.744 ± 0.058	2.144 ± 0.058	1.875 ± 0.079	4.468 ± 0.082	0.525 ± 0.036	0.649 ± 0.091	2.638 ± 0.089	–	–	–	0.156 ± 0.029	33.493 ± 0.499
NGC 1389	4.667 ± 0.083	4.498 ± 0.082	2.039 ± 0.067	2.897 ± 0.105	4.778 ± 0.120	1.141 ± 0.054	1.360 ± 0.128	4.611 ± 0.103	1.331 ± 0.067	0.209 ± 0.061	3.182 ± 0.132	1.131 ± 0.081	22.639 ± 0.183
NGC 1426	4.885 ± 0.090	4.744 ± 0.058	2.444 ± 0.028	3.371 ± 0.096	5.170 ± 0.095	1.160 ± 0.049	1.981 ± 0.081	4.338 ± 0.089	1.045 ± 0.046	0.373 ± 0.042	2.796 ± 0.157	1.693 ± 0.085	23.222 ± 0.215
NGC 3818	4.875 ± 0.121	4.331 ± 0.081	2.714 ± 0.045	3.452 ± 0.157	4.747 ± 0.068	1.292 ± 0.037	1.623 ± 0.112	5.753 ± 0.156	0.952 ± 0.036	0.753 ± 0.043	2.429 ± 0.173	1.171 ± 0.071	22.596 ± 0.194
NGC 4339	4.381 ± 0.087	4.020 ± 0.128	2.537 ± 0.035	3.657 ± 0.080	4.833 ± 0.062	1.202 ± 0.028	1.507 ± 0.065	4.588 ± 0.118	0.356 ± 0.049	0.248 ± 0.046	3.227 ± 0.166	1.054 ± 0.048	21.816 ± 0.204
NGC 4365	4.701 ± 0.209	4.450 ± 0.113	2.594 ± 0.086	3.938 ± 0.273	5.126 ± 0.057	1.202 ± 0.045	0.952 ± 0.083	7.518 ± 0.281	1.432 ± 0.064	0.994 ± 0.068	3.209 ± 0.150	0.982 ± 0.070	22.207 ± 0.176
NGC 4371	4.270 ± 0.191	4.299 ± 0.084	2.774 ± 0.069	3.260 ± 0.110	3.925 ± 0.125	0.912 ± 0.050	1.495 ± 0.065	5.093 ± 0.137	1.496 ± 0.061	0.934 ± 0.060	3.666 ± 0.157	0.971 ± 0.039	22.111 ± 0.197
NGC 4377	4.469 ± 0.100	–	2.453 ± 0.067	3.225 ± 0.128	4.612 ± 0.088	1.214 ± 0.035	1.663 ± 0.068	4.440 ± 0.130	1.164 ± 0.048	0.428 ± 0.046	1.784 ± 0.158	0.778 ± 0.073	22.849 ± 0.187

This paper has been typeset from a TeX/LaTeX file prepared by the author.